

Magnetic susceptibility measurements as a function of temperature and frequency I: inversion theory

R. Egli

Ludwig-Maximilians Universität, Departement für Geo- und Umweltwissenschaften, Theresienstrasse 41, 80333 München, Germany.
E-mail: egli@geophysik.uni-muenchen.de

Accepted 2008 December 16. Received 2008 November 30; in original form 2008 June 30

SUMMARY

Magnetic measurements as a function of temperature and time are commonly used to reconstruct the volume distribution of superparamagnetic (SP) particles. Knowledge of the temperature dependence of the magnetic moments and the anisotropy energies is necessary for a correct interpretation of the measurements. Temperature dependences are usually derived from bulk magnetic properties. The magnetic properties of small particles, however, are strongly influenced by surface effects related to low-temperature oxidation, reduced coordination of surface spins and interactions with surrounding molecules. These effects are difficult to quantify, especially in rocks and sediments. To address this problem, a method for reconstructing the magnetic properties of weakly interacting assemblages of SP particles is presented. The method is based on the inversion of magnetic susceptibility measurements performed for a range of temperatures at different frequencies. The redundancy of the measurements is used to obtain estimates of the abovementioned temperature dependences, the effective interaction field and the pre-exponential factor in Néel–Brown relaxation theory without using any *a priori* assumptions on the magnetic properties of the particles. The inversion method was successfully tested on numerical samples representing typical susceptibility measurements of natural and artificial samples. Susceptibility inversion results can provide new insights in the magnetic properties of fine particles relevant in palaeo- and environmental magnetism.

Key words: Environmental magnetism; Rock and mineral magnetism.

1 INTRODUCTION

Single domain (SD) iron minerals with a distribution of blocking temperatures below and above room temperature occur in a variety of rocks and sediments of interest for palaeo- and environmental magnetism studies. Ultrafine iron oxides and sulphides are an active component of the iron cycle and therefore reflect palaeoenvironmental conditions (Thompson & Oldfield 1986; Cornell & Schwertmann 2003; Evans & Heller 2003). This mineral fraction is also important for understanding post-depositional processes (Tarduno 1995; Schwartz *et al.* 1997) and pedogenesis. Most attention has been devoted to ultrafine magnetite (Fe_3O_4) or maghemite ($\gamma\text{-Fe}_2\text{O}_3$), which has been recognized as the main source of susceptibility enhancement in soils and palaeosols (Evans & Heller 1994; Maher 1998). Although magnetic particles with blocking temperatures <400 K do not carry a useful palaeomagnetic signal, they provide a good analogue of stable SD remanence carriers in the study of alteration processes. For example, low-temperature oxidation of magnetite is a diffusion-limited process that can be scaled to laboratory time using 10 nm magnetite particles (Tang *et al.* 2003).

Antiferromagnetic (af) minerals such as haematite (Fe_2O_3), goethite (FeOOH) and ferrihydrite ($\text{Fe}_5\text{HO}_8\cdot 4\text{H}_2\text{O}$) are generally

much more abundant than magnetite in sediments, with typical concentrations of 1–10 weight per cent (Cornell & Schwertmann 2003; van der Zee *et al.* 2003). Because of the lower saturation magnetization of af iron oxides (0.5–2 per cent of magnetites, depending also on grain size) and one order of magnitude higher coercivities, the contribution of af and ferrimagnetic nanoparticles to the magnetic susceptibility can be equally important. The quantification of iron oxides and oxyhydroxides provides an insight into the iron biogeochemical cycle (Kappler & Straub 2005), whereby non-destructive magnetic measurements can be adopted for this purpose (Banerjee 2006). However, because of the inherent difficulty in characterizing samples containing SP minerals with a broad distribution of compositions and blocking temperatures, there is a lack of quantitative studies on their occurrence and properties in rocks and sediments.

This paper is the first of two that will address the quantitative magnetic characterization of SP minerals using susceptibility measurements as a function of temperature and frequency. Various methods have been developed to reconstruct the grain size distribution (GSD) or the energy barrier distribution (EBD) of magnetic particles. All methods are based on measuring the effect of temperature and/or time on a remanent or an induced magnetization. For example, the joint distribution of grain sizes and microcoercivities

can be calculated from alternating field demagnetizations of partial thermoremanences (Dunlop & West 1969) and direct field demagnetization curves of isothermal remanent magnetizations acquired at different temperatures (Jackson *et al.* 2006). One of the first successful applications of these techniques was the reconstruction of the GSD of acicular magnetite in tuff samples from the Yucca Mountain (Worm & Jackson 1999; Jackson *et al.* 2006).

On the other hand, measurements of the induced magnetization in a weak direct or alternating field as a function of temperature are widely used to calculate the average energy barrier of superparamagnetic (SP) particles (Dormann *et al.* 1997). The first step toward the inversion of susceptibility measurements using a polynomial representation of the volume distribution can be dated back to Stephenson (1971). A complete reconstruction of the volume distribution from magnetic susceptibility measurements was first reported in Jonsson *et al.* (1997) for a diluted maghemite ferrofluid. The volume distribution reconstruction was based on Néel's theory of superparamagnetism with the assumption of isolated uniaxial particles with temperature independent magnetic properties, identical microcoercivities and a broad distribution of energy barriers. Later, Shcherbakov & Fabian (2005) proposed a suitable correction for analysing susceptibility measurements of weakly interacting Stoner–Wohlfarth (SW) particles with known temperature dependences of saturation magnetization and microcoercivity. Their correction proved to be effective when analysing Tiva Canyon tuff samples and concentrated ferrofluid suspensions.

The analysis of susceptibility measurements has two intrinsic advantages over other magnetic characterization methods. First, the out-of-phase susceptibility is relatively insensitive to temperature-dependent phenomena that are not related to thermally activated switching of magnetic moments. This property can be used to characterize samples containing mixtures of particles with different domain states, as they often occur in nature, whereby the signal produced by non-SP particles is efficiently suppressed. Some limitations occur with large amounts of multidomain particles, since a small out-of-phase susceptibility component is produced by electron hopping and/or tunnelling in stoichiometric magnetite below the Verwey temperature (Balanda *et al.* 2005), and by vacancy-mediated relaxation near room temperature in low-Ti magnetite (Walz *et al.* 2003). Since these phenomena are observed in large crystals that can be removed from sediments by magnetic extraction, quantitative investigation of SP minerals in natural samples based on susceptibility measurements is possible. The second advantage of susceptibility measurements is that of providing data sets that are redundant with respect to the EBD. This redundancy offers the possibility of testing the validity of current magnetic relaxation models, as well as providing additional information on the temperature dependence of the intrinsic magnetic properties of SP particles.

All of grain-size reconstruction methods require knowledge of the temperature dependence of the magnetic moment m and the microcoercivity H_K of the particles or an equivalent parameter combination. The simplest case relevant to rocks and sediments is represented by elongated magnetite particles, where the SW model predicts both m and H_K to be proportional to the saturation magnetization (Stoner & Wohlfarth 1948). The temperature dependences of m and H_K are then given by $M_s \propto (1 - T/T_c)^\gamma$, where T_c is the Curie temperature and γ an appropriate exponent (Dunlop & Özdemir 1997). Accordingly, temperature dependences can be neglected in interpreting measurements below room temperature for all minerals having a large T_c . A generalization of this conclusion, based on the SW model, can be misleading. Several processes are responsible for

important changes of the magnetic properties at low temperatures in small particles. For example, SP magnetite is small enough to undergo low-temperature oxidation at room temperature (Tang *et al.* 2003). Low-temperature oxidation is a diffusion-controlled process that produces a cation-deficient surface layer with spin glass-like properties. This layer becomes magnetic at low temperature and might be exchange-coupled with the particle's core (e.g. Kodama *et al.* 1996). The magnetism of small ferrimagnetic nanoparticles is also affected by a surface layer of disordered spins (e.g. Labaye *et al.* 2002; Lu *et al.* 2007; Shendruk *et al.* 2007). The surface spins seem also to become pinned if magnetic nanoparticles are coated with organic molecules (Berkowitz *et al.* 1975), a process that can naturally occur in sediments. All these effects can introduce significant differences between the magnetic properties of fine particles and bulk materials, including strong temperature dependences of some magnetic properties. Whereas surface anisotropy and interactions with coating molecules are expected to be important only in very small particles having a relatively high number of surface spins, low temperature oxidation effects are important also in much larger particles of interest in palaeointensity studies.

The magnetism of af nanoparticles is controlled by the incomplete compensation between atomic spins of the A and B sublattices (Néel 1961). Incomplete compensation might arise from random defects and/or from the surface of the particles. In both cases, the uncompensated spins produce a residual grain-size-dependent magnetic moment m_p that can be several times larger than the ordinary moment related to the saturation magnetization of the bulk material. The uncompensated moment m_p is equivalent to that of a SP ferromagnetic particle; therefore, this phenomenon is often called superantiferromagnetism. The temperature dependence of m_p and the related microcoercivity is poorly understood. The few data available suggest that superantiferromagnetism is far more complicated than superparamagnetism (Seehra & Punnoose 2001).

The temperature dependences of m and H_K can be derived directly from measurements of hysteresis loops, provided that all magnetic moments are blocked, and saturation can be reached. Goethite and fine-grained haematite, however, cannot be saturated in maximum fields typically attainable during hysteresis measurements (Rochette *et al.* 2005). Furthermore, magnetic moments are progressively unblocked as the temperature is raised, and GSD must be taken into account to interpret the measurements. Current methods for calculating the GSD require in turn $m(T)$ and $H_K(T)$ to be known, so that some *a priori* assumptions are needed to model SP particles. The scope of this paper is to circumvent this problem by providing a method to invert susceptibility measurements without the need of *a priori* assumptions about the magnetic properties of the particles. The method is a refinement of the analysis of susceptibility data proposed by Svedlindh *et al.* (1997), which is integrated by the correction introduced by Shcherbakov & Fabian (2005) for weak magnetostatic interactions.

A brief outline of the paper is given to conclude this introduction. Sections 2 and 3 provide a review of current knowledge on forward models of temperature- and frequency-dependent susceptibility measurements. The forward model is extended to explicitly account for the temperature dependence of the intrinsic magnetic properties of the particles and for the effect of weak magnetostatic interactions. Section 4 sets the theoretical background for the full inversion of susceptibility measurements. A general method is then implemented to invert susceptibility data acquired with widespread measurement protocols. The inversion method is checked against simulated measurements of realistic SP assemblages. Critical assumptions underlying the forward susceptibility model are briefly

discussed in Section 5, with particular emphasis on the validity of the Néel–Brown relaxation theory and the applicability of the model to heterogeneous particle mixtures. In a follow-up paper, the validity of the forward model will be discussed in detail, addressing the problem of interacting particles characterized by mixed anisotropy and low-damping relaxation modes. A list of recurring symbols used in mathematical expression throughout this paper is given in Table 1.

2 DYNAMIC LINEAR SUSCEPTIBILITY OF SW PARTICLES

The magnetization M of an ensemble of magnetic particles in a small sinusoidal field $H_0 \cos(\omega t)$ of frequency $f = \omega/(2\pi)$ is given by the Fourier series

$$M(t) = \sum_{k=0}^{\infty} H_0^k [\chi'_k \cos(k\omega t) - \chi''_k \sin(k\omega t)], \quad (1)$$

with coefficients χ'_k and χ''_k (García-Palacios 2000). If the sinusoidal field is not biased by a constant field, the system has inversion symmetry, and all even Fourier coefficients are zero. Furthermore, $\chi = \chi'_1 - i\chi''_1$ is the linear dynamic susceptibility of the particles. If $H_0 \rightarrow 0$ is a sufficiently small field, all terms with $k > 1$ can be neglected: $\chi' = \chi'_1$ and $\chi'' = \chi''_1$ are then called the in-phase and the quadrature (or out-of-phase) susceptibilities.

Analytical or numerical expressions for the linear susceptibility are obtained from the solution of the Fokker–Plank equation that describes the magnetic moment vector of a particle subjected to thermal activations in a small field. A notable effort has been undertaken to obtain both analytical and numerical solutions of the Fokker–Plank equation for assemblages of non-interacting particles, which are exhaustively described in a review by García-Palacios (2000). The first analytical solution of the problem for isolated SW particles has been obtained by Néel (1949), using some approximations described in the next section. This solution has been adopted since then in studies of superparamagnetic particles in rocks and sediments (e.g. Mullins & Tite 1973; Shcherbakov & Fabian 2005). Exact solutions of the Fokker–Plank equation are far more complex than the original result of Néel (1949). An analytical expression for the linear susceptibility has been obtained by Shliomis & Stepanov (1993) and Raikher & Stepanov (1997). Their solution, hereafter called the Shliomis–Stepanov–Raikher (SSR) model, is formally similar to the result of Néel (1949), as it will be shown later. The SSR model has been later verified by numerical solution of the stochastic Landau–Lifshitz–Gilbert equation (García-Palacios & Lázaro 1998).

Magnetostatic interactions within SP particle assemblages represent a further complication, since they affect the linear dynamic susceptibility in a complex, non-linear manner. An extensive review of the interaction problem is given by Jönsson (2004). A simple first-order correction of Néel's solution for weakly interacting uniaxial particles is described in Shcherbakov & Fabian (2005) and will be adopted here to extend the SSR solution to the case of weak interactions.

The SSR model and its adaptation to the case of weakly interacting particles are described in the following paragraphs, providing a forward problem solution for linear susceptibility calculations. A slightly different notation than in the original literature will be used here, so that a formal identity with the well-known Néel (1949) solution is maintained. Furthermore, unlike in the original literature, the

Table 1. List of important recurring symbols.

Symbol	First defined in	Description
b	Section 3.1	Proportionality constant for χ_{ns}
β	Section 2.1	Boltzmann factor
β_0	Section 2.1	Blocking condition
C	Section 2.3	Volume concentration of particles
C_p	Eq.30	Paramagnetic constant
χ	Section 2	Magnetic susceptibility (complex number)
χ'	Section 2	Real (or in-phase) component of χ
$\hat{\chi}'$	Section 4.3	χ' reconstructed from χ''
χ''	Section 2	Imaginary (or quadrature) component of χ
χ_f	Eq.18	Frequency dependence of χ'
χ_{SD}	Section 2.1	Single domain susceptibility (SW)
χ_{ns}	Section 2.1	Non-switching susceptibility
χ'_{sw}	Section 2.1	Switching susceptibility (in-phase)
χ_0	Section 2.2	SD susceptibility in the SSR model
$\delta\chi'$	Section 4.3	$\hat{\chi}' - \chi'$
$\langle \delta\chi'^2 \rangle$	Eq.34	Quadratic mean of $\delta\chi'$
$\Delta\chi'_{\text{sw},i}$	Section 4.3	$\chi'_{\text{sw}}(r_i) - \chi'_{\text{sw}}(r)$
E	Section 2.1	Energy barrier at temperature T
E_0	Section 3.2	Energy barrier at reference temperature T_0
ε	Section 3.2	Temperature dependence of E
$\hat{\varepsilon}$	Section 4.2	Reconstructed ε
$\tilde{\varepsilon}$	Section 4.2	$\hat{\varepsilon}$, stabilized against divergence at $T \rightarrow 0$
f	Section 2	Frequency of the measuring field
Φ	Section 4.4	$\langle \delta q^2 \rangle \langle \delta\chi'^2 \rangle$
G	Section 3.4	Energy barrier distribution (EBD)
\hat{G}	Eq.35	Reconstructed energy barrier distribution
h_i	Section 2.3	H_i/H_K
H_i	Section 2.3	Mean interaction field
H_K	Section 2.1	Microcoercivity
h_0	Section 3.2	h_i at reference temperature T_0
\hat{h}_0	Section 4.4	Estimated h_0
η	Section 2.2	Correction factor for χ_{ns}
η_r	Eq.3	Damping constant
J	Section 2.3	Correction function for weak interactions
k	Section 3.2	Temperature dependence of H_K
K	Eq.9	Kernel function
\tilde{K}	Eq.10	Approximation of K
κ	Eq.20	Temperature dependence of χ_{ns}
λ	Section 3.5	Ratio of logarithmic frequencies
\mathbf{m}, m	Section 2.1	Magnetic moment (vector and module)
M	Eq.1	Magnetization
M_s	Section 2.1	Saturation magnetization
M_{rs}	Section 3.1	Saturation remanence
μ	Section 2.1	Temperature dependence of m
μ_s	Section 2.3	Saturation magnetization of a particle
p	Section 5.1	Stretching exponent
q	Eq.14	Scaling function for χ''
Q	Section 4.2	Polynomial approximation of Q
$\langle \delta q^2 \rangle$	Eq.29	Mean quadratic differences between $q(f_j)$
r	Section 3.2	Temperature dependence of m/H_K
\hat{r}	Section 4.3	Reconstructed r
ρ	Section 4.3	Relative error of the reconstructed r
s	eq.25	Temperature scaling function
T	Section 2.1	Absolute temperature
T^*	Section 4.2	Scaled temperature
T_0	Section 3.2	Reference temperature
τ_0	Eq.3	Pre-exponential factor
$\hat{\tau}_0$	Section 4.4	Estimated τ_0
τ'_0	Section 5.1	τ_0 equivalent in a stretched Néel–Arrhenius law
V	Section 2.1	Volume of a particle
w	Section 3.4	$2\pi\tau_0 f$
ω	Section 2	$2\pi f$
ζ	Section 4.3	Damping factor
ξ	Eq.5	Correction factor for χ_{sw}
ξ_b	Section 3.4	$\xi(\beta_0)$

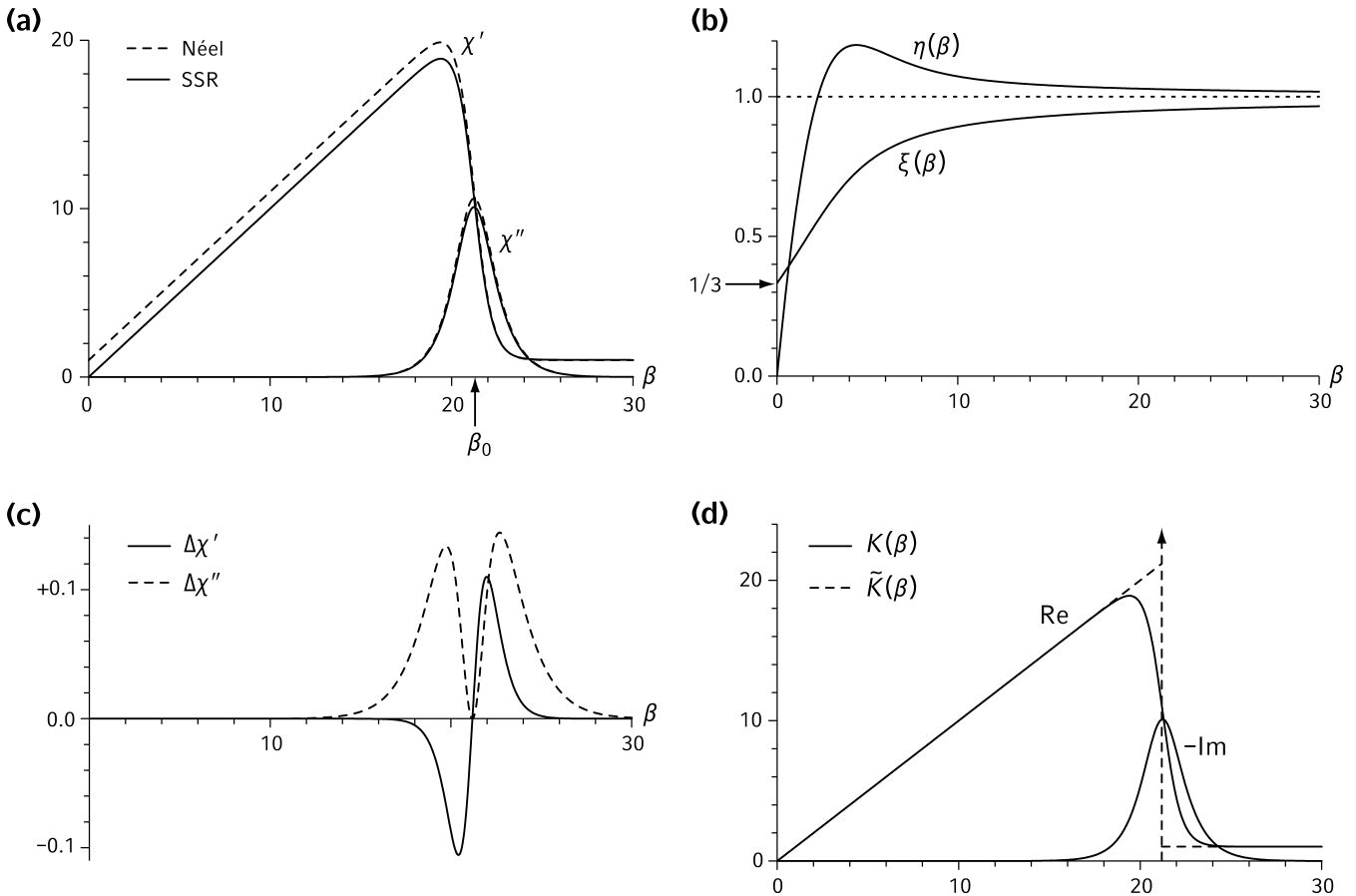


Figure 1. (a) Real (χ') and imaginary (χ'') components of the linear magnetic susceptibility as a function of β , according to Néel's model (dashed lines) and the SSR model (solid lines). The parameters used for calculations are $\tau_0 = 10^{-10}$ s and $f = 1$ Hz. The arrow indicates the blocking condition $\beta_0 = -\ln(\tau_0\omega)$. (b) Correction factors used to formulate the SSR model using the Néel formalism. (c) Differences $\Delta\chi'$ and $\Delta\chi''$ between the real and the imaginary components of the susceptibility calculated using τ_0 in (3) and the same expression for τ_0 where β was replaced by β_0 . (d) Real (Re) and Imaginary (Im) components of the kernel function (9) (solid lines) and the approximation (10) used for wide energy barrier distributions (dashed lines). The arrow indicates the Dirac δ -function extending to infinity.

dependence of the model parameters on the absolute temperature T is treated explicitly.

2.1 Néel's solution for non-interacting SW particles

The susceptibility of randomly oriented, non-interacting SW particles was calculated by Néel (1949) by solving the kinetic equation, which describes the time dependence of the magnetic moment of a uniaxial particle in a small field. He assumed that the motion of the magnetic moment vector can be ascribed to two distinct mechanisms: (1) the instantaneous rotation of the moment toward the applied field and (2) thermally activated transitions of the magnetic moment between equilibrium states. The first mechanism is responsible for what will be called here the non-switching susceptibility χ_{ns} . The single-domain susceptibility $\chi_{\text{SD}} = 2M_s/(3H_K)$ of randomly oriented SW particles with saturation magnetization M_s and microcoercivity H_K coincides with χ_{ns} when $T = 0$. In a uniaxial particle, the second mechanism refers to switching of the magnetic moment between the two equilibrium orientations parallel to the easy axis. The contribution of moment switching to the linear susceptibility is called here switching susceptibility χ_{sw} and is obviously zero if the magnetic particles are in a blocked state. The total linear susceptibility $\chi = \chi_{\text{ns}} + \chi_{\text{sw}}$ at any temperature is

the sum of the two contributions. Néel's solution can be written as

$$\chi(T, f) = \chi_{\text{SD}} \left[\frac{\beta}{1 + i\tau_0\omega e^\beta} + 1 \right], \quad (2)$$

where τ_0 is the pre-exponential factor of the Néel–Brown relaxation model, and the Boltzmann factor $\beta = E/(k_B T)$ is defined as the ratio of the particle's energy barrier E in zero field and the thermal energy $k_B T$. The energy barrier of a SW particle is $E = \mu_0 m H_K / 2 = KV$, where m is the magnetic moment, H_K is the so-called microcoercivity, V is the volume and K is the anisotropy constant. A relatively sharp transition from a blocked state, characterized by $\chi = \chi_{\text{SD}}$, to an unblocked state of the particles occurs at $\beta_0 = -\ln(\tau_0\omega)$, with $15 \leq \beta_0 \leq 22$ for the usual range of measuring frequencies ($f = 1$ Hz–1 kHz). The transition is marked by a maximum of the real and imaginary part of χ (Fig. 1a).

The pre-exponential factor of the Néel–Brown relaxation model is a complicated function of H_K and β . The following expression valid for large energy barriers $\beta \geq 5$ in a zero field can be obtained from a solution reported in Dormann *et al.* (1996):

$$\tau_0 \approx \frac{1}{2\mu_0\gamma_0 H_K} \sqrt{\frac{\pi}{\beta}} \left[\eta_r \mu + \frac{1}{\eta_r \mu} \right], \quad (3)$$

where $\gamma_0 = 8.794 \times 10^{10} \text{ T}^{-1} \text{ s}^{-1}$ is the electronic gyromagnetic

ratio, η_r is a dimensionless damping constant between 0.01 and 1 and $\mu = m(T)/m(0)$ is the temperature dependence of the magnetic moment (see Appendix A1). Usually the variation of τ_0 with temperature is neglected, as it is expected to be small compared with the effect of the exponential term e^β in the Néel–Brown relaxation formalism. The validity of this assumption for susceptibility models can be tested by replacing β in (3), with the constant value $\beta_0 \approx 20$ corresponding to the blocking condition does not produce notable differences in a plot of $\chi(\beta)$ obtained from (2) (Fig. 1c). As final remark, it should be noted that the Néel–Brown relaxation model is based on the assumption that the magnetization of the particle is uniform. This has been verified experimentally on a single cobalt nanoparticle (Wernsdorfer *et al.* 1997a), so that (3) can be assumed to hold for sufficiently small particles.

2.2 The Shliomis–Stepanov–Raikher model

The most important simplification underlying Néel’s solution (2) is based on the formal separation between non-switching and switching processes as described in Section 2.1. Moment switching is assumed to occur between two equilibrium configurations where the moment is parallel to the easy axis, whereby this is strictly true only at $T = 0$. Similarly, the equilibrium orientation of the magnetic moment in a weak field, used to obtain χ_{ns} , is calculated by neglecting thermal perturbations. In a real system at $T > 0$, the magnetic moment is continuously perturbed, giving raise to significant effects when the thermal energy $k_B T$ becomes comparable to the energy barrier of the particle. The SSR model takes these effects into account and provides a solution for the linear susceptibility of isolated, uniaxial particles, which is valid over the entire range of temperatures. Maintaining Néel’s formalism, the SSR solution for the linear susceptibility of a random assemblage of non-interacting SW particles can be written as

$$\chi(T, f) = \chi_0 \left[\frac{\beta \xi}{1 + i\tau_0 \omega e^\beta} + \beta(1 - \xi) \right], \quad (4)$$

where $\chi_0 = \chi_{SD}$ for SW particles, and

$$\xi(\beta) = \frac{\int_{-1}^1 z^2 e^{\beta z^2} dz}{\int_{-1}^1 e^{\beta z^2} dz} = \frac{e^\beta}{\sqrt{\pi\beta} \operatorname{erfi}(\sqrt{\beta})}, \quad (5)$$

is a correction factor with $\operatorname{erfi}(z) = \operatorname{erf}(iz)/i$ being the imaginary error function (see Appendix A2 for a formal derivation from the solution given by García-Palacios 2000). The validity of (4) is limited to the so-called low-frequency case, where transverse relaxation phenomena are negligible. This is usually the case for $\omega \lesssim 1$ MHz, well below frequencies required for resonance phenomena (García-Palacios 2000).

The SSR solution (4) is formally equivalent to eq. (2) if $\xi(\beta)$ is interpreted as a correction factor that accounts for thermal perturbations of the moment vector from equilibrium. Accordingly, χ_{sw} and χ_{ns} in Néel’s model are corrected by the factors ξ and $\eta = \beta(1 - \xi)$, respectively (Fig. 1b). The function $\xi(\beta)$ increases monotonically with β from $\xi(0) = 1/3$, which represents the case of a fully randomized moment vector, to $\xi(\infty) = 1$. The latter asymptotic solution corresponds to $T = 0$ and describes the case of the magnetic moment being aligned with the easy axis of the particle, as assumed by Néel (1949). The interpretation of η is less straightforward, since $\eta(\beta)$ is not monotonic. Again, the asymptotic case $\eta(\infty) = 1$ corresponds to Néel’s calculation of the equilibrium orientation of the magnetic moment in a weak field. As the temperature increases from $T = 0$, η initially increases to a maximum value of 1.185 at $\beta \approx 4.38$. The associated increase of χ_{ns}

can be interpreted as the effect of a larger probability of finding the magnetic moment vector to be aligned with the applied field due to random fluctuations of the moment. As the temperature increases further, the randomization effect of thermal fluctuations prevails, and $\eta(0) = 0$ indicates a complete random state.

A comparison of Néel’s solution with the SSR model shows the effect of the correction factors ξ and η , which is particularly evident for the in-phase susceptibility of the particles in the unblocked state $\beta < \beta_0$ (Fig. 1a).

2.3 Correction for magnetostatic interactions

Let C be the volume concentration of interacting particles made of a material with bulk saturation magnetization μ_s . A system of strongly magnetic, non-touching particles, such as a ferrofluid, is dominated by so-called dipolar interactions, where H_i is approximated by the sum of the dipolar fields produced by all magnetic moments. On the other hand, if the particles are touching, exchange coupling between spins at contact points can occur, giving raise to exchange interactions (Mørup *et al.* 2007). Exchange interactions dominate in pure powders of af nanoparticles, since the magnetization is much smaller than in ferrimagnetic materials.

Interactions affect the energy barrier of the particles and break the original uniaxial symmetry. This in turn modifies the relaxation time, depending on the energy barrier and on its symmetry. The dipolar interaction strength is usually expressed by the ratio between the interaction energy $\mu_0 m H_i$ and the energy barrier $\mu_0 m H_K/2$ in a zero external field. This ratio is thus proportional to $h_i = H_i/H_K$. Numerical solutions of the Landau–Lifshitz equation for interacting uniaxial particles show that χ depends on h_i and on the damping constant η_r in a complicated manner (Berkov & Gorn 2001; Jönsson 2004). Shcherbakov & Fabian (2005) provided an analytical approximation for a fixed interaction field $h_i \ll 1$ being aligned with the easy axes of all particles, which is correct for the high-damping case $\eta_r \gg 1$. In their solution, χ_{sw} is decreased by an extent accounted by the correction factor $\operatorname{sech}^2(2\beta h_i)$.

Although numerical solutions reported in the literature correspond to frequencies in the 10 MHz range, the analytical solution of Shcherbakov & Fabian (2005) does not take into account the natural distribution of orientations and amplitudes of H_i , which characterize a random system of particles. A generalization of this solution for random interacting systems will be discussed in a follow-up paper, where it will be shown that the correction factor $\operatorname{sech}^2(2\beta h_i)$ should be replaced with an appropriate function of the form $J(2\beta h_i)$. The term ‘weak interactions’ is used here to denote interaction fields that do not significantly affect the anisotropy energy of the particles. Experiments on magnetite nanoparticles show that the blocking temperature of dispersed particles and thus the anisotropy energy, becomes independent of C when $r/d > 6$, where r is the distance between the centres of the particles, and d is their diameter (Bae *et al.* 2007). This limit corresponds to a volume concentration $C \approx (d/r)^3 = 0.0046$. Large sets of randomly placed and randomly oriented moments generate an interaction field distribution whose width depends on C . A typical distribution width of 0.002 μ_s is obtained for $C \approx 0.0046$ (Egli 2006). Using this result and $\mu_s = 480$ kA m⁻¹ and $\mu_0 H_K \approx 80$ mT for the equidimensional magnetite particles studied in Bae *et al.* (2007), $h_i \leq 0.015$ is obtained as a general upper limit for the validity range of the mean field model of Shcherbakov & Fabian (2005).

The linear susceptibility of weakly interacting particles is calculated by applying the abovementioned correction to the SSR model,

obtaining:

$$\chi(T, f) = \chi_0 \left[\frac{\beta\xi}{1 + i\tau_0\omega e^\beta} J(2\beta h_i) + \eta \right]. \quad (6)$$

In the following, eq. (6) is taken as the solution of the forward model for the susceptibility of identical, randomly oriented, weakly interacting SW particles.

3 THE FORWARD MODEL FOR UNIAXIAL PARTICLES

A further generalization of the linear susceptibility model is obtained by considering a set of uniaxial particles characterized by a distribution of energy barriers with identical temperature dependences. The calculation of the magnetic susceptibility for such particles defines the forward problem discussed in this section.

3.1 Susceptibility of identical uniaxial particles

Consider a set of identical magnetic particles with uniaxial anisotropy and randomly oriented easy axes. For the sake of calculating the magnetic susceptibility, the particles are fully described by their magnetic moment $m(V, T)$ in zero field and the microcoercivity $H_K(V, T)$, whereby both parameters depend on the particle's volume V and the absolute temperature T . The simplest model for m and H_K (Stoner & Wohlfarth 1948) is based on the assumption that the magnetization is homogenous in the entire particle (Fig. 2a). In this case, $m(V, T) = V\mu_s(T)$ and $H_K = H_K(T)$, with μ_s being the saturation magnetization of the bulk material. Surface effects (e.g. Labaye *et al.* 2002; Shendruk *et al.* 2007) and uncompensated spin moments (Mørup *et al.* 2007) are two possible factors that produce an inhomogeneous magnetization in ferri- and antiferromagnetic nanoparticles, respectively (Figs 2b and c). In such cases, the SW model might no longer be applicable.

The general case of uniaxial particles can be understood by considering the relationship between the non-switching and the switching field susceptibilities on one hand and the hysteresis loop of the particle assemblage in a blocked state on the other (Fig. 3). At $T = 0$, the non-switching susceptibility of non-interacting particles coincides with the slope of the hysteresis loop at $H = 0$, since irreversible processes take place only when $|H|$ exceeds the smallest switching field. On the other hand, magnetic moment switching in uniaxial particles occurs between two equilibrium states, which collectively define the saturation remanence M_{rs} at $T = 0$. The fixed shape of SW hysteresis loops (Fig. 3a) imposes the condition $\chi_{ns}/(\eta\chi_0) = 1$, as implicitly assumed in (6). This is not the case for particles with a generic hysteresis loop, where M_{rs} and the loop slope at $H = 0$ are independent of each other (Fig. 3b), defining values of $b = \chi_{ns}/(\eta\chi_0)$ that are $\neq 1$. Accordingly, the SSR model of eq. (6) can be adapted to such cases by writing

$$\chi(T, f) \approx \chi_0 \left[\frac{\beta\xi}{1 + i\tau_0\omega e^\beta} J(2\beta h_i) + b\eta \right], \quad (7)$$

with $\chi_0 \propto M_{rs}/H_K$. A rigorous approach to the problem would require a new calculation of the correction terms η and ξ , based on a detailed model of the moment reversal mechanism. Since this is not generally possible, the same correction factors as in eq. (4) are used. The error introduced by this approximation is expected to be small over a wide range of temperature, because ξ and η are close to unit for $\beta > 5$.

3.2 Temperature dependences in the SW model

The susceptibility of SW particles depends on the parameters E , χ_{SD} and h_i , which are functions of the temperature T and the particle volume V . In the following, it is assumed that the magnetic moment m and the microcoercivity H_K can be expressed as the product of a function of V (volume dependence) and a function of T (temperature dependence). The separation of the volume and temperature dependences does not imply any loss of generality for the case of identical particles, since they all have the same volume. However, it might represent a restriction in case of samples containing particles with different volumes (Figs 2d and e). Nevertheless, the separation of volume and temperature dependences provides the most general case that allows for a full inversion of susceptibility measurements. The implications of this assumption will be discussed in Section 5.

Let now introduce the temperature dependences $\mu(T) = m(T)/m(T_0)$ of m and $k(T) = H_K(T)/H_K(T_0)$ of H_K , respectively, with $\mu(T_0) = k(T_0) = 1$ for a reference temperature T_0 . Then, $E = E_0\varepsilon(T)$, with $\varepsilon = \mu k$ being the temperature dependence of E , and $E_0 = E(T_0)$. Furthermore, $\chi_0 \propto r(T)$, with $r = \mu/k$ describing the temperature dependence of the SD susceptibility. Using the definitions of μ and ε , it is evident that $r(T_0) = \varepsilon(T_0) = 1$.

The temperature dependence of h_i can be calculated from first-principles considerations about the origin of the interaction field. Ferrimagnetic particles are usually strongly magnetic, and the weak interaction limit $h_i \ll 1$ discussed in Section 2.3 already excludes the case of contacting particles. The interaction field acting on one particle is then given by the sum H_d of all dipole fields produced by the surrounding particles, with $H_d \propto m$ (Fig. 2f). The temperature dependence of h_i is then expressed by $h_i = h_0 r(T)$, with $h_0 = h_i(T_0)$.

3.3 Temperature dependences in the general case

Knowledge of the temperature dependences of all parameters in (7) relies on a detailed model describing the magnetization of a thermally activated particle in a small field. The SW model predicts χ_0 to be proportional to m/H_K . This is expected to hold also for the general uniaxial case, provided that H_K is defined so that the energy barrier is $E = \mu_0 m_0 H_K/2$, where m_0 is the magnetic moment in a zero field.

The non-switching susceptibility χ_{ns} is controlled by the dependence of the magnetic energy on perturbations produced by a small external field. If the magnetization is homogeneous, the magnetic energy is expressed by the sum of two terms: the anisotropy energy, which is proportional to H_K , and the Zeeman energy, which is proportional to the applied field H . Additional terms are required to describe the magnetic energy of a non-homogeneous magnetization, resulting in a more complicated temperature dependence of χ_{ns} . A general solution for χ_{ns} can obviously not be formulated, however, it is reasonable to expect a similarity with the SW model for all cases where the magnetization is not excessively inhomogeneous. Considering that χ_{ns} is small compared with the bulk susceptibility in the unblocked range (e.g. Fig. 1), a precise estimate of its temperature dependence is not essential. Therefore, the best possible approximation of the general uniaxial case is obtained by assuming that both χ_{ns} and χ_{sw} have identical temperature dependences given by $r \approx \mu/k$.

Dipole interactions between antiferromagnetic particles are usually negligible, because of their weak magnetizations and high coercivities. Therefore, magnetic interactions between such particles arise practically from the exchange coupling between contact points

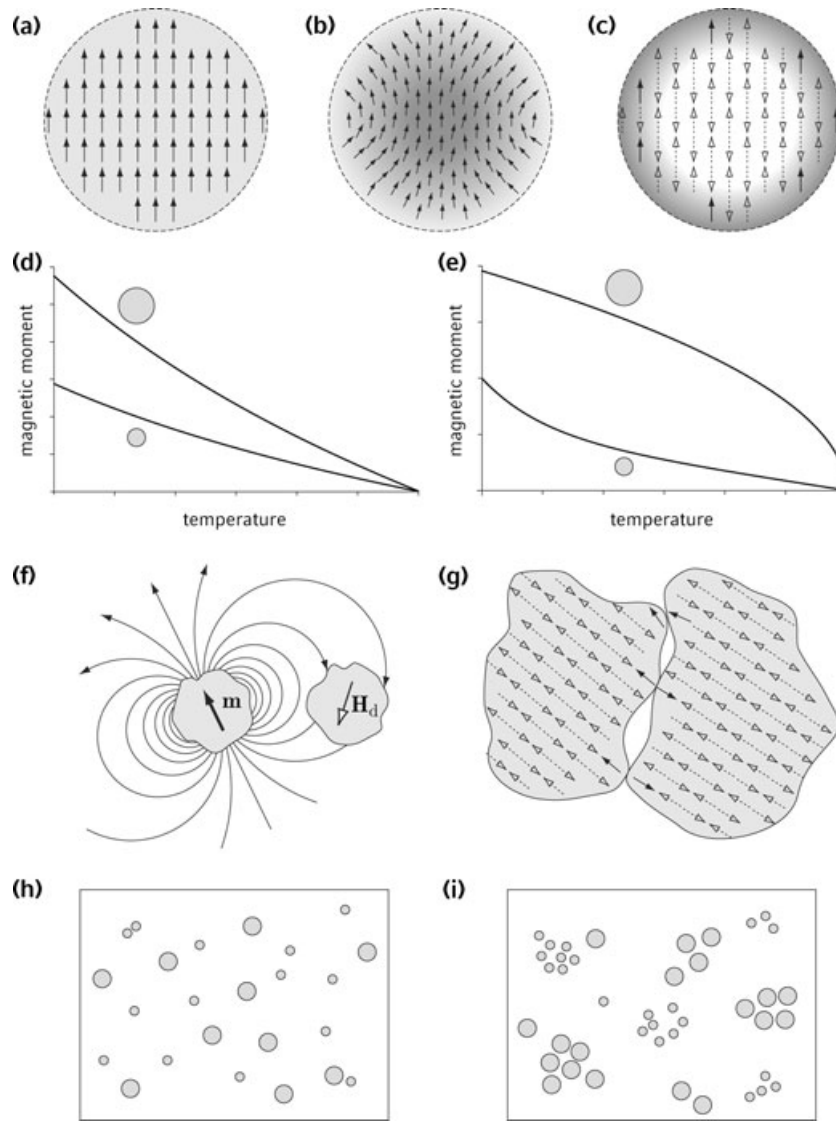


Figure 2. Schematic summary of factors affecting the properties of SP and SD particles, grouped into magnetization homogeneity (a–c), temperature dependence effects (d and e), magnetostatic interactions (f and g) and sample heterogeneity (h and i). (a) The magnetization of SW particles is homogeneous in the entire volume of the particle. (b) Hedgehog-like spin structure in a ferromagnetic nanoparticle, produced by surface anisotropy. (c) The magnetic moment of af nanoparticles is produced by uncompensated atomic spins (filled arrows), in this case due to the surface of the particle. Shading in (a)–(c) is qualitatively proportional to the vertical component of the magnetization. (d) Two particles whose magnetic moments are different but have the same temperature dependence. (e) Two particles whose temperature dependence of the magnetic moment is controlled by the volume. (f) and (g) Magnetostatic interactions between particles are produced by a dipolar field associated with their magnetic moment (f) or by exchange coupling between contact points (filled arrows) (g). (h) In a homogeneous sample, the position of each particle is completely random, and interactions occur between any kinds of particles. (i) Heterogeneities occur when similar particles are grouped into clusters. In this example, small and large particles form distinct clusters and magnetostatic interactions within the two groups of clusters may differ.

(Hansen *et al.* 2000; Fig. 2g). The temperature dependence of exchange coupling interactions is more complicated than for the dipolar case. Fine antiferromagnetic particles have a magnetic moment that arises from incomplete magnetic compensation between sublattices. Néel (1961) hypothesized three possible cases that would produce an uncompensated moment proportional to n^α , where n is the number of spins and $\alpha = 1/3, 1/2$ and $2/3$, respectively. The case of $\alpha = 2/3$ corresponds to a magnetic moment that is simply proportional to the surface of the particle (Fig. 2c). One can reasonably assume the number of contact points between any pair of particles to be proportional to their surface. In case of few contact points, the strength of the exchange coupling can be considered proportional to their number. Therefore, H_i is also proportional to

the surface of the particles, and $H_i \propto m$ is obtained, as for the case of dipole interactions. This simple result is not valid for the other two cases discussed by Néel (1961), since a similar reasoning would give $H_i \propto m^{1/2}$ or $H_i \propto m^{3/4}$. For sake of simplicity, and considering the uncertainties affecting a mean field treatment of interactions, $H_i \propto m$ is used in the following to model the temperature dependence of both dipolar and exchange interactions.

3.4 Distribution of energy barriers

Consider now a large set of particles with a joint distribution of volumes and microcoercivities. Since it is not possible to reconstruct the joint distribution of V and H_K from susceptibility

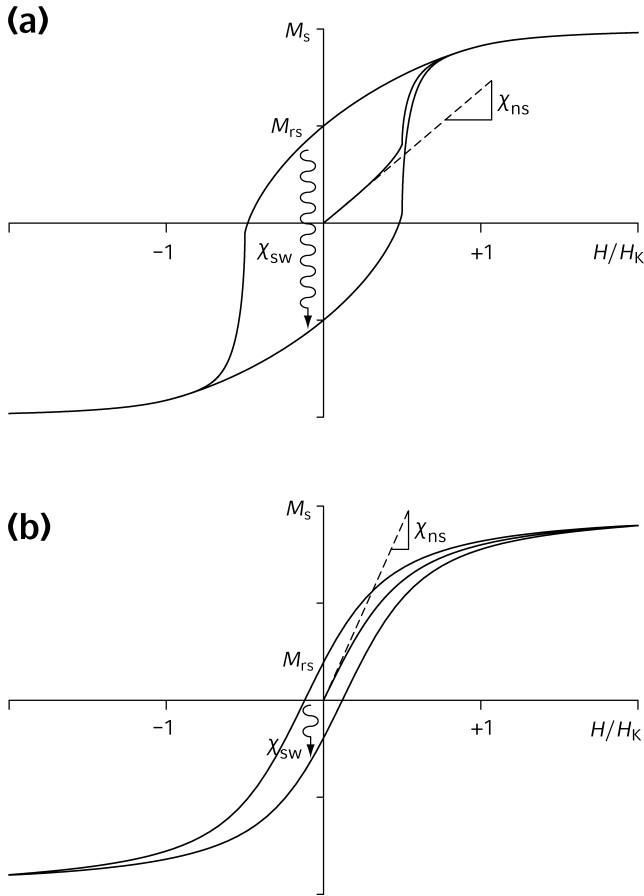


Figure 3. Schematic representation of the relation between the hysteresis loop at 0 K and the susceptibility of non-interacting SD particles. The non-switching susceptibility χ_{ns} coincides with the slope of the loop at $H = 0$ (dashed lines). The switching susceptibility χ_{sw} is related to a change of the remanent state of the sample (arrows) and is therefore proportional to the saturation remanence M_{rs} . (a) Randomly oriented Stoner–Wohlfarth particles ($M_{rs}/M_s = 0.5$) and (b) particles characterized by $M_{rs}/M_s < 0.5$. Compared with (a), χ_{ns} in (b) is larger and χ_{sw} is smaller.

measurements alone, SP particles are at best characterized by the distribution $G(E_0)$ of energy barriers $E_0 = E(T_0)$ at a reference temperature T_0 . More precisely, $G(E_0)dE_0$ is defined as the contribution to $\chi_0(T_0)$ in (7) from all particles with energy barriers within the interval $[E_0, E_0 + dE_0]$. In the following, $G(E_0)$ is referred to as the energy barrier distribution (EBD) of the particles. It is important to realize that $G(E_0)$ differs from the EBD definition used to analyse magnetization curves, such as in Jackson *et al.* (2006). There, the EBD represents a contribution to the magnetization, instead of χ_0 . With both definitions of EBD, additional *a priori* assumptions are needed to obtain the volume distribution, as explained in Appendix A3.

Depending on how the particles are distributed in the sample's volume, the effective interaction field seen by one particle might be statistically correlated with its properties, such as the volume. This is, for example, the case for samples containing isolated clusters of particles, where the particles in one cluster are different from those in another cluster (Fig. 2i). This could represent a common situation in sediments, where the growth of authigenic iron minerals is influenced by a heterogeneous distribution of chemical conditions. However, since no information is generally available on such

details, it is assumed in the following that no correlation exists between the particle's magnetic properties and their position in the sample. An equivalent statement is that the distribution of particles is totally random, and that the effective interaction field is a constant parameter.

Given the assumptions discussed above, the susceptibility of a large set of particles with EBD $G(E_0)$ is calculated by weighted integration of (7) over E_0 :

$$\chi(T, f) = br(T) \int_0^\infty G(E_0)\eta(\beta)dE_0 + r(T) \int_0^\infty G(E_0)K(\beta, f)J(2\beta h_0 r)dE_0, \quad (8)$$

with $\varepsilon = \varepsilon(T)$, $r = r(T)$, $\beta = E_0\varepsilon/(k_B T)$, and the kernel function

$$K(\beta, f) = \frac{\beta \xi(\beta)}{1 + i\tau_0 \omega e^\beta}. \quad (9)$$

Eqs (8) and (9) represent the forward model for calculating $\chi(T, f)$ from a known distribution $G(E_0)$ of energy barriers. The inverse problem consists in calculating the unknown $G(E_0)$, $r(T)$, $\varepsilon(T)$, b and h_0 from $\chi(T, f)$.

A first important simplification in the theoretical handling of the forward model is obtained for the case of $G(E_0)$ being a broad distribution, where the sense of 'broad' is specified as follows. Since E_0 is positive, the EBD is a positive distribution function that is best considered on a logarithmic scale with $G(\log E_0) = E_0 G(E_0) \ln 10$. A measure unitless measure for the broadness of the EBD is then given by the standard deviation of $\log E_0$. In synthetic samples, the lowest standard deviation, 0.2, is observed for ferritin particles. Since the ferrihydrite core of full-loaded ferritin is precisely constrained by the structure of the protein shell, one can reasonably assume 0.2 to be a practical lower limit for the standard deviation of $\log E_0$. For comparison, standard deviation values of ≈ 0.4 are obtained from the EBD reconstruction of maghemite ferrofluids (Jonsson *et al.* 1997) and ≈ 0.5 for pedogenic particles in Chinese palaeosols (Liu *et al.* 2005). If $\text{sd}(\log E_0) \geq 0.2$, the kernel function in (9) can be replaced by following approximation

$$\tilde{K}(\beta) = \beta \xi(\beta) H(-\beta - \ln w) + i \frac{\pi}{2} \xi_b \ln w \delta(\beta + \ln w), \quad (10)$$

where $H(x)$ is the Heaviside unit step function, $\delta(x)$ is the Dirac δ -function, $w = \tau_0 \omega$ is the dimensionless measurement frequency and $\xi_b = \xi(-\ln w) \approx 1$. This expression for the kernel function with $\xi = 1$ was used by Néel (1949) to describe SP particles with a distribution of volumes and is therefore referred to as Néel's approximation in the following. If Néel's approximation is compared with the exact solution in the case of a lognormal distribution of energy barriers characterized by $\sigma(\log E_0) = 0.2$, one finds that the difference between the two solutions is < 1 per cent for $\chi''(T, f)$ and < 0.2 per cent for $\chi'(T, f)$ (Fig. 4). Since larger errors are involved in some assumptions underlying eq. (8), Néel's approximation can in practice replace the exact solution.

Using (8) and (10), the forward model simplifies to

$$\chi''(T, f) = -\frac{\pi \xi_b r(T)}{2\varepsilon(T)} k_B T \ln w G[-k_B T \ln w / \varepsilon(T)] \times J[2h_0 r(T) \ln w], \quad (11)$$

for the out-of-phase susceptibility. Using the variable substitution $\beta = E_0\varepsilon/(k_B T)$,

$$\chi'_{sw}(T, f) = r(T) \frac{k_B T}{\varepsilon(T)} \int_0^{-\ln w} G(\beta k_B T / \varepsilon) \beta \xi(\beta) J(2\beta h_0 r) d\beta \quad (12)$$

is obtained for the in-phase switching susceptibility.

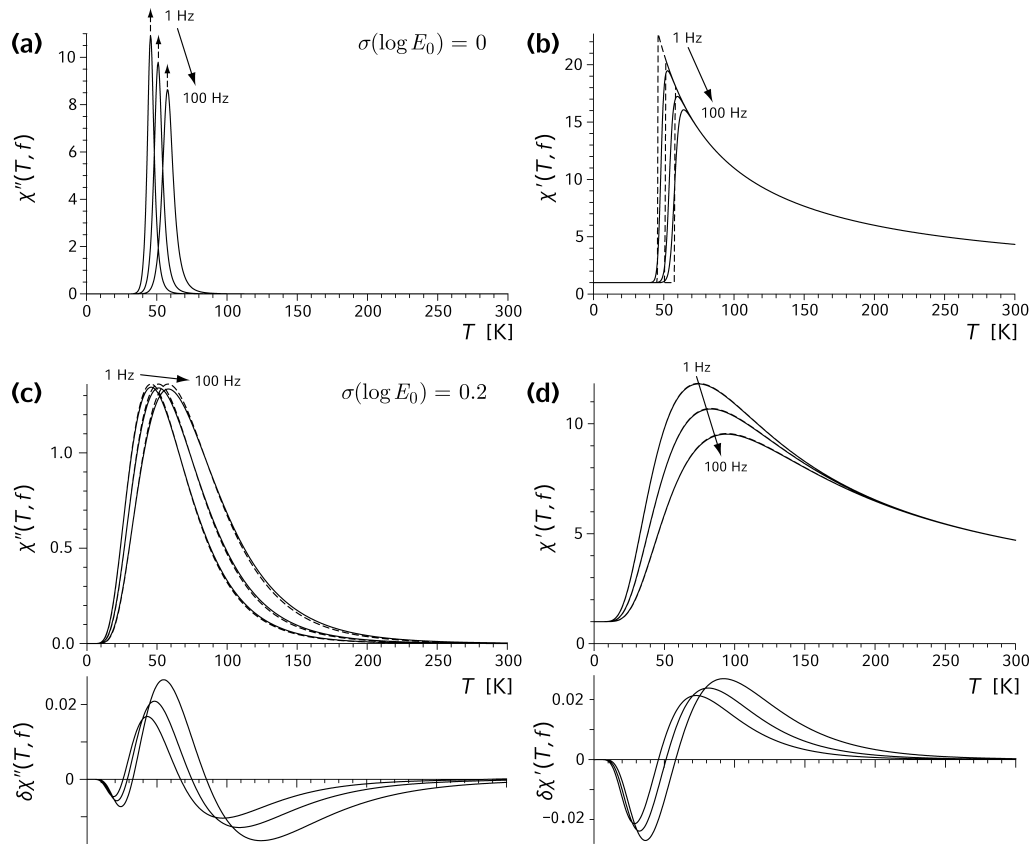


Figure 4. Comparison between the susceptibility of non-interacting SW particles at five different frequencies calculated using the exact forward model (eqs 8 and 9, solid lines), and Néel's approximation (eqs 11 and 12, dashed lines). (a) and (b) Imaginary and real component, respectively, for identical, randomly oriented particles characterized by $E = 10^3 k_B$. Dashed arrows indicate Dirac's d -function. (c) and (d) Imaginary and real component, respectively, of randomly oriented SW particles characterized by a lognormal distribution of energy barriers (median: $10^3 k_B$, dispersion parameter: 0.2). The difference between Néel's approximation (dashed lines) and the exact solution (solid lines) is plotted below. All cases have been calculated using $\tau_0 = 10^{-10}$ s, $h_0 = 0$, $r(T) = \varepsilon(T) = 1$ and $f = 1, 10, 100$ Hz.

3.5. Universal relations between susceptibility measurements

Susceptibility measurements as a function of temperature and frequency are redundant, since well-defined relations exist between the in-phase and the quadrature component, as well as between measurements performed at different frequencies. These relations provide the key for the inversion of susceptibility measurements and are therefore discussed extensively in the following.

Let $\chi(x; y)$ represent susceptibility measurements performed for a range of values x and a fixed parameter y . Then, $\chi(T; f)$ is a measurement of the susceptibility as a function of temperature performed at a fixed frequency f , and $\chi(f; T)$ is a measurement of the susceptibility as a function of frequency performed at a fixed temperature T . If the parameters $r(T)$, $\varepsilon(T)$, b , h_0 and τ_0 are known, any series of measurements of $\chi(T; f)$ or $\chi(f; T)$ completely suffice for reconstructing $G(E_0)$, provided that the first argument of χ extends over a range that is wide enough to include measurements of each magnetic particle in the blocked as well as in the unblocked state. Complete measurements of $\chi(f; T)$ are hardly possible since they require a range of frequencies that extends over > 10 decades. Moreover, the validity range of the SSR model limits the maximum frequencies that can be used to < 1 MHz. Therefore, measurements of the type $\chi(T; f)$ are most used and will be considered in the following. In the remaining part of this section it will be show that any

curve $\chi(T; f)$ can be calculated from a measurement of $\chi''(T; f_0)$ or $\chi'(T; f_0)$ with a frequency f_0 , knowing $r(T)$, $\varepsilon(T)$, h_0 , b and τ_0 .

Eq. (11) can be solved with respect to $G(E_0)$, obtaining

$$G(E_0) = \frac{2\chi''(u; f)}{\pi \xi_b r(u) E_0 J[2h_0 r(u) \ln w]}, \quad (13)$$

where u is the solution of $u/\varepsilon(u) = -E_0/(k_B \ln w)$. Eqs (11) and (13) can now be used to prove that the function

$$q(T) = \frac{\chi''(u; f)}{r(u) \xi(-\ln w) J[2h_0 r(u) \ln w]} \quad (14)$$

is independent of f if u is the solution of

$$\frac{u}{\varepsilon(u)} = \lambda \frac{T}{\varepsilon(T)}, \quad (15)$$

with $\lambda = \ln(2\pi \tau_0 f_0) / \ln(2\pi \tau_0 f)$ and an arbitrary chosen reference frequency f_0 (see Appendix A4). The function $q(T)$ can be obtained from any plot of the right-hand side of (14) by rescaling the temperature axis according to (15). If ε is a constant, (15) simplifies to $u = \lambda T$, which underlies the well-known scaled plots of χ'' versus the scaled temperature $T \ln(2\pi \tau_0 f)$ used to estimate τ_0 (e.g. Jonsson *et al.* 1997).

The definition of $q(T)$ can be used to calculate any $\chi''(T; f)$ from a measurement of $\chi''(T; f_0)$ at a given frequency f_0 . If (13)

is substituted into (12), following relation between $\chi'_{\text{sw}}(T; f)$ and $\chi''(T; f)$ is obtained:

$$\chi'_{\text{sw}}(T, f) = \frac{2}{\pi \xi_b} \int_0^{-\ln w} \chi''(u, f) \xi \beta \frac{r(T)}{r(u)} \frac{J[2h_0 r(T) \beta]}{J[2h_0 r(u) \ln w]} d\beta, \quad (16)$$

with u being the solution of

$$\frac{u}{\varepsilon(u)} = -\frac{T}{\varepsilon(T)} \frac{\beta}{\ln w}. \quad (17)$$

Eq. (16) is a version of the so-called Kramers-Krönig relation between the real and the imaginary part of the complex susceptibility (Toll 1956; García-Palacios 2000). Another important relation, the so-called $\pi/2$ -law, is obtained from the derivative of (16) with respect to f :

$$\chi_f(T) = \frac{\partial \chi'(T; f)}{\partial \log f} = -\frac{2}{\pi} \chi''(u, f), \quad (18)$$

where χ_f is the frequency dependence of the in-phase susceptibility (see Appendix A5). This expression is an approximation of the general $\pi/2$ -law (Shcherbakov & Fabian 2005), which holds for the case where $G(E_0)$ is a broad distribution in the sense discussed in Section 3.4. Experimental evidence for a violation of this law therefore indicates that either $G(E_0)$ is a narrow distribution or susceptibility was not measured in the linear range. For the sake of completeness, it should be mentioned that the parameter $\chi_{\text{fd}} = 100 \chi_f / \chi'$ is also called frequency dependence of susceptibility in the literature and used as grain size indicator. The interpretation of χ_{fd} in terms of grain distributions is discussed in Worm (1998).

Although (16) represents a compact expression to calculate $\chi'_{\text{sw}}(T; f)$ from $\chi''(T; f)$, it is of little practical use since it requires solving the non-linear eq. (17) with respect to the integration variable. Following explicit solution

$$\begin{aligned} \chi'_{\text{sw}}(T, f) &= -\frac{2 \ln w}{\pi \xi_b T} \int_0^T \chi''(u, f) \frac{r(T) \varepsilon(T)}{r(u) \varepsilon(u)} \left[1 - u \frac{\varepsilon'(u)}{\varepsilon(u)} \right] \xi I du, \\ \xi &= \xi \left[-\frac{u \varepsilon(T)}{T \varepsilon(u)} \ln w \right], \\ I &= \frac{J \left[2h_0 r(T) \frac{u \varepsilon(T)}{T \varepsilon(u)} \ln w \right]}{J[2h_0 r(u) \ln w]}, \end{aligned} \quad (19)$$

is obtained from (16) and (17) using an appropriate variable substitution (see Appendix A6). Similarly, the non-switching susceptibility is $\chi_{\text{ns}} = b\kappa$, where κ is the temperature dependence of χ_{ns} , given by

$$\begin{aligned} \kappa(T) &= \frac{2r(T)}{\pi \xi_b} \int_0^\infty \frac{\chi''(u, f)}{ur(u)} \left[1 - u \frac{\varepsilon'(u)}{\varepsilon(u)} \right] \eta I du, \\ \eta &= \eta \left[-\frac{u \varepsilon(T)}{T \varepsilon(u)} \ln w \right], \\ I &= J^{-1} [2h_0 r(u) \ln w]. \end{aligned} \quad (20)$$

The main result of this section is a set of three equations (14, 19 and 20), which fully specifies the relations between $\chi'(T; f)$, $\chi''(T; f)$ and $\chi_f(T)$. This will be the starting point for the construction of a general method to invert $\chi(T; f)$ and obtain the unknown parameters $r(T)$, $\varepsilon(T)$, h_0 and $G(E_0)$.

4 INVERSION OF SUSCEPTIBILITY MEASUREMENTS

It has been shown in Section 3 that measurements of $\chi(T; f)$, at different frequencies are redundant with respect to the reconstruc-

tion of the EBD. One can therefore ask if it is possible to use this redundancy to actually calculate the parameters $r(T)$, $\varepsilon(T)$, h_0 and τ_0 , instead of using arbitrary assumptions. The answer to this question is not trivial since it depends on whether the solutions of the inverse problem for the different parameters are independent from each other. This is the case only if any parameter combination produces a forward model that is different from that obtained from other combinations. Alternatively, there could be a finite number of parameter combinations sharing the same forward model $\chi(T; f)$: in this case, the inverse problem has more than one solution. Both cases require that the inverse problem is not underdetermined and has a finite number of distinct solutions. The existence of discrete inverse problem solutions is discussed in the following, before a suitable inversion method is developed.

4.1 Existence of discrete solutions of the inverse problem

A strict proof for the universal existence of discrete solutions of the inverse problem is difficult. A local proof for a given combination of parameters can be obtained by showing that a small change of any of these parameters affects $\chi(T; f)$ in a way that cannot be mimicked by any combination of small changes of the other parameters. Since $G(E_0)$ does not appear explicitly in any of the relations between measurements of $\chi(T; f)$ discussed in Section 3 (specifically eqs 14 and 19 and 20), it will not be involved in the calculation of the other model parameters. Therefore, a proof of linear independence is required only for $r(T)$, $\varepsilon(T)$, h_0 and τ_0 . The effect on $\chi(T; f)$ produced by infinitesimal changes $\delta r(T)$, $\delta \varepsilon(T)$, δh_0 and $\delta \tau_0$ with respect to an initial choice of parameters can be analysed by considering the difference $\Delta_p \chi$ in susceptibility obtained by replacing one parameter p with $p + \delta p$. Since δp is infinitesimal, the problem is linearized using $\Delta_p \chi = \chi_p \delta p$, where χ_p is the partial derivative of χ with respect to p . Because of the weak dependence of χ on τ_0 , χ_τ indicates the derivative with respect to $\ln \tau_0$. The four model parameters will then define four functions $\chi_p \delta p$ that represent the effect of a small change of each parameter on $\chi(T; f)$. The parameters are independent if it can be shown that $\chi_p \delta p$ are linearly independent functions. This is the case if the Wronskian determinant W of the functions $\chi_p(f)$ fulfils the condition

$$W(\chi_\varepsilon, \chi_r, \chi_h, \chi_\tau) \neq 0, \quad (21)$$

for a range of temperatures and frequencies (see Appendix A7 and Sansone 1991). The Wronskian determinant is indeed a positive function of T and f similar in shape to $\chi''(T; f)$, and (21) is therefore fulfilled in the range of temperatures where $\chi''(T; f)$ is significantly above the noise level of the measurements (Fig. 5b). Since (21) only requires δp not to be a function of the frequency, it is in principle possible to solve the inverse problem for τ_0 being a function of the temperature. This would provide an interesting possibility to check existing calculations of τ_0 . Unfortunately, it is not possible to obtain such a result on real measurements, because W contains derivatives of χ with respect to the frequency up to the third order. Second and third-order derivatives with respect to f are extremely small and well below the detection limit of measurements performed over the usual ranges of frequencies extending over — two to three decades. Since the calculation the model parameters could eventually rely on such high-order derivatives, a different proof for the independence of $\chi_p \delta p$ is necessary, which is based only on measurable quantities. A suitable proof has been found only for the case where h_0 and τ_0 are constants and is explained in the following.

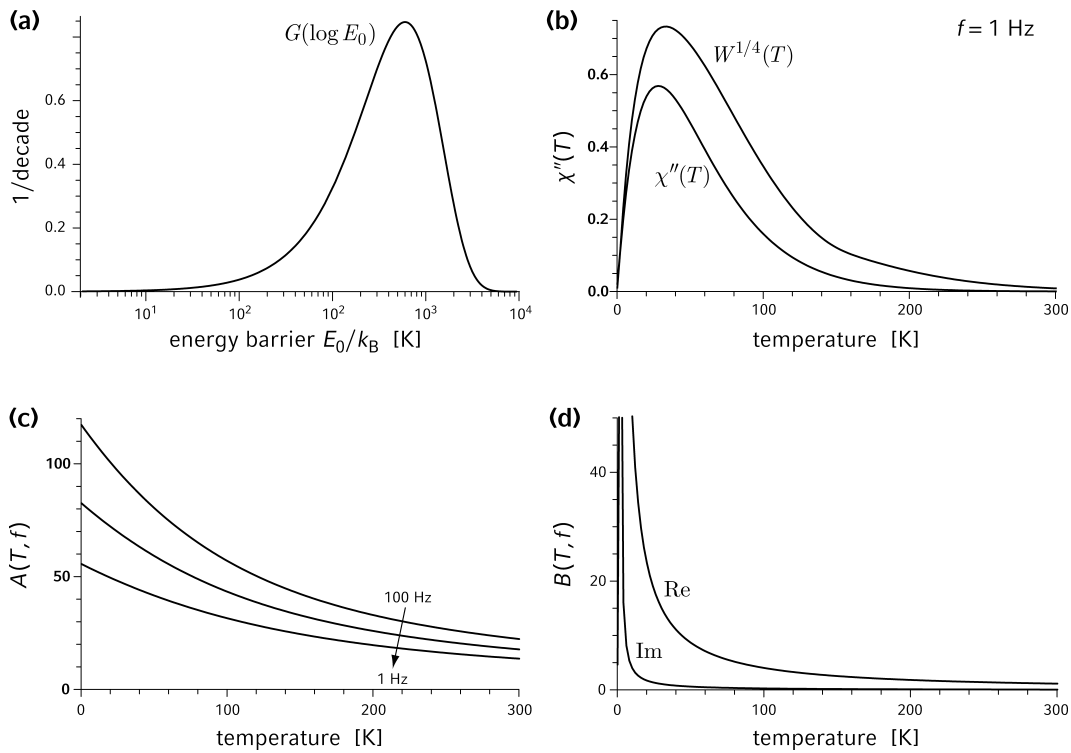


Figure 5. Numerical proof of the existence of discrete inverse problem solutions for an assemblage of SW particles characterized by $r(T) = \varepsilon(T) = 1$, $h_0 = 0.003$, the energy barrier distribution plotted in (a) and $\tau_0 = 10^{-10}$ s. (b) Comparison between the Wronskian determinant W and the imaginary susceptibility component χ'' for $f = 1$ Hz. $W^{1/4}$ is plotted instead of W for units consistency with χ'' . (c) Frequency dependence of the function A and (d) temperature dependence of the real and imaginary component of the function B defined in (23).

If the functions $\chi_p \delta p$ are linearly dependent, the equation

$$\chi_\varepsilon \delta \varepsilon + \chi_r \delta r + \chi_h \delta h_0 + \chi_\tau \delta \ln \tau_0 = 0 \quad (22)$$

has at least one solution with respect to $\delta \varepsilon(T)$, $\delta r(T)$, δh_0 and $\delta \tau_0$. After some algebraic manipulations explained in Appendix A7, it can be shown that a solution of (22) exists if

$$A(f) = \frac{\chi'_h \chi''_r - \chi''_h \chi'_r}{\chi'_\tau \chi''_r - \chi''_\tau \chi'_r}, \quad B(T) = \frac{\chi_{h,f} \chi_r - \chi_h \chi_{r,f}}{\chi_{\tau,f} \chi_r - \chi_\tau \chi_{r,f}} \quad (23)$$

are constant with respect to the specified variable over the entire range of measured temperatures and frequencies. This is impossible, as shown with an example in Figs 5c and d, since (23) is over determined with respect to the model parameters. Hence, changes in $\chi(T; f)$ produced by $\delta \varepsilon(T)$, $\delta r(T)$, δh_0 and $\delta \ln \tau_0$ are linearly independent.

Qualitative arguments for the independence of the model parameters are provided by the example of Fig. 6, where $\chi(T; f)$ was calculated for a typical assemblage of SP grains with $r = \varepsilon = 1$ and $h_0 = 0$, and successively perturbed by replacing each of these parameters by a different function or value. It can be seen on this example that each parameter has a different effect on $\chi(T; f)$. Changes of $\varepsilon(T)$ affects the temperature dependences of both the real and the imaginary part of $\chi(T; f)$, similarly to what can be obtained by modifying the EBD (Figs 6a and b). However, the effects of $\varepsilon(T)$ and $G(E_0)$ are not identical and can always be distinguished. On the other hand, $r(T)$ mainly affects the temperature dependence of $\chi'(T; f)$ and much less that of $\chi''(T; f)$ (Fig 6c and d). Indeed, plots of $\chi''(T; f)$ calculated using different models of $r(T)$ are brought to a good overlap, simply by multiplying $\chi''(T; f)$ with an appropriate constant. Magnetostatic interactions reduce the overall amplitude of

$\chi(T; f)$, whereby this effect is more pronounced for the imaginary component (Figs 6e and f). Interactions also affects the frequency dependence of the peak amplitude of $\chi''(T; f)$, and this effect is considered a distinctive feature of interactions in relaxing systems (Jönsson 2004). However, a similar effect is obtained if r depends on the temperature, so that its interpretation in weakly interacting particles depend both on $r(T)$ and h_0 .

Now that the existence of inverse problem solutions has been demonstrated, a method allowing the effective calculation of the model parameters is developed in the following. A possible inversion approach is based on implementing model functions for $r(T)$ and $\varepsilon(T)$, whose shapes are controlled by a set of function parameters. Non-linear minimization methods could then be used to find a combination of parameters that minimizes the difference between forward model and measurements. This approach has been successfully used in coercivity analysis, where coercivity distributions are modelled using probability density functions (Heslop *et al.* 2002; Egli 2003). However, unlike coercivity distributions, temperature dependences are controlled by a number of processes that cannot be easily approached using model functions. Therefore, a different solution of the inverse problem is developed here, which is not based on pre-defined functions or any other arbitrary assumption on $r(T)$ and $\varepsilon(T)$.

The inversion procedure will be illustrated using the numerical example shown in Fig. 7, which simulates susceptibility measurements of a collection of randomly oriented, weakly interacting SW particles with an arbitrary but realistic choice of the model parameters $G(E_0)$, $r(T)$, $\varepsilon(T)$, h_0 and τ_0 . The exact forward model eqs (8) and (9) were used to calculate a list (T_k, χ_{k_j}) of simulated out-of-phase and in-phase linear susceptibility measurements at

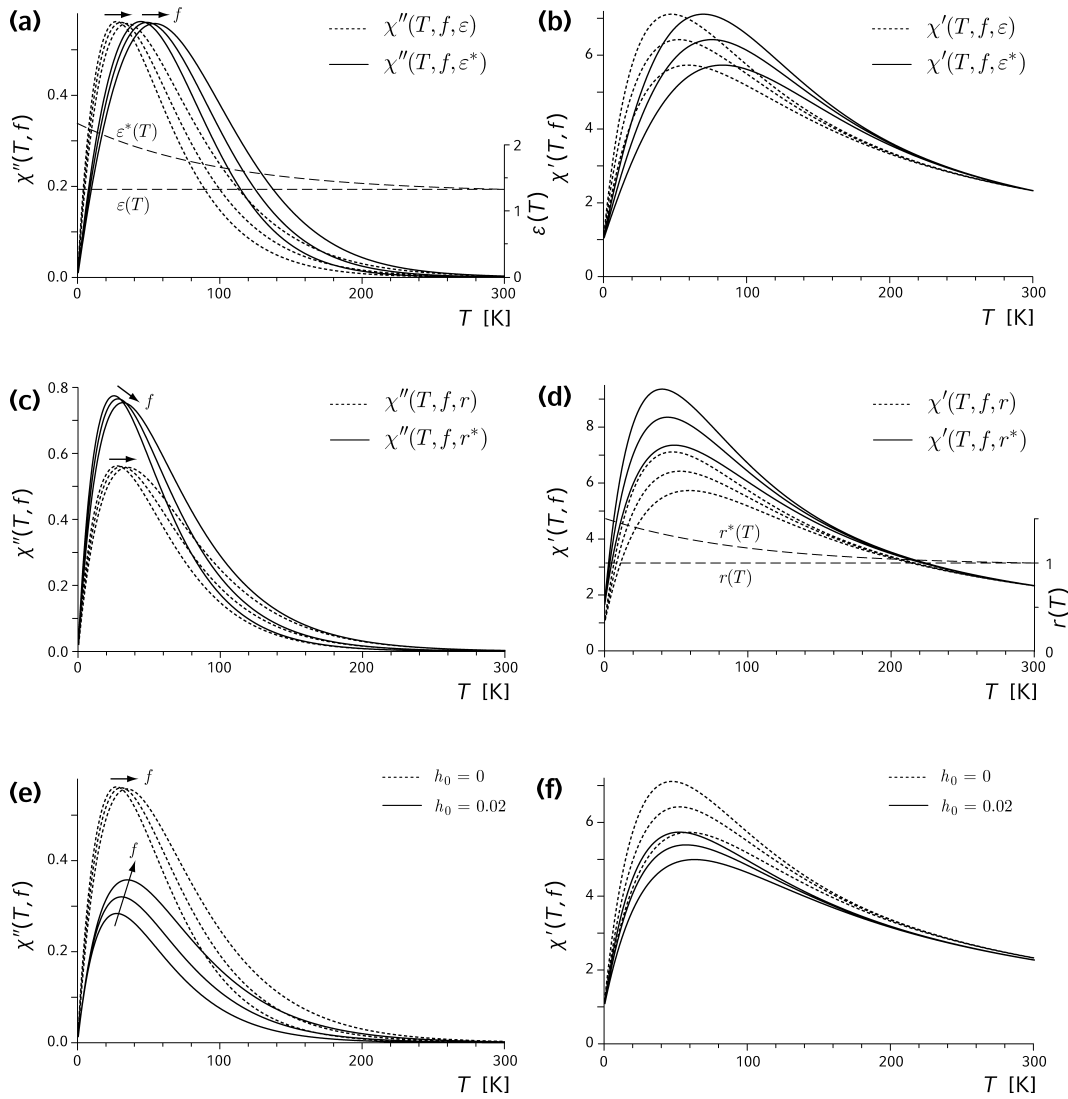


Figure 6. Influence of $r(T)$, $\varepsilon(T)$ and h_0 on the imaginary (left-hand plots) and real (right-hand plots) susceptibility components of randomly oriented SW particles with energy barrier distribution given in Fig. 5a, calculated for $f = 1, 10$ and 100 Hz. The original model with $r(T) = \varepsilon(T) = 1$ and $h_0 = 0$ is shown by the dashed lines; solid lines correspond to the susceptibility obtained after replacing $\varepsilon(T) = 1$ with $\varepsilon^*(T)$ (a and b), $r(T) = 1$ with $r^*(T)$ (c and d) and $h_0 = 0$ with $h_0 = 0.02$ (e and f). Arrows indicate the shift of the maximum in $\chi''(T, f)$ with increasing frequency.

discrete temperatures T_k and frequencies f_j , with $\chi_{kj} = \chi(T_k; f_j)$ and $\chi_{kj} = \chi'_{kj} - i\chi''_{kj}$.

4.2 Reconstruction of $\varepsilon(T)$

A graphic representation of $q(T)$ is obtained by plotting each out-of-phase measurement (T_k, χ''_{kj}) on modified coordinates given by

$$T_{kj}^* = T_k^2 / u_{kj}, \quad (24)$$

$$q_{kj} = q_j(T_{kj}^*) = \frac{\chi''_{kj}}{r(T_k) \xi(-\ln w_j) J[2h_0 r(T_k) \ln w_j]},$$

where u_{kj} is the solution of (15) with $T = T_k$ and $f = f_j$. Assume for now that $r(T)$, h_0 and τ_0 are known. It is then possible to find a function $\varepsilon(T)$ such that eqs (14) and (15), or the graphical counterpart (24), are fulfilled for all measured frequencies and temperatures. Once a correct solution of $\varepsilon(T)$ is found, the functions $q_j(T)$ calculated from measurements performed at different frequencies f_j are identical. This means that one can always find a set of scaled

temperatures T_{kj}^* , such that the curves defined by the coordinates (T_{kj}^*, q_{kj}) overlap. A perfect overlap is expected if the parameters $r(T)$, h_0 and τ_0 are chosen correctly and if the measurements are free of errors. Once the T_{kj}^* are determined experimentally, the coefficients u_{kj} are calculated using the first equation in (24). Each of the calculated u_{kj} must satisfy (15), where the only unknown is the function $\varepsilon(T)$.

Before solving (15) with respect to $\varepsilon(T)$, it is useful to note that λ is a number close to unit for typical frequency ranges used experimentally. For example, $\lambda \approx 0.92$ if the frequencies differ by one order of magnitude in the range between 0.1 Hz and 1 kHz. Eq. (15) has the trivial solution $u = T$ if $\lambda = 1$, and one can easily see that $u/T \rightarrow 1$ as $\lambda \rightarrow 1$. Therefore, any solution of (15) for the limit case of $\lambda \rightarrow 1$ can be written as

$$\frac{u(T, f)}{T} = 1 + (\lambda - 1)s(T), \quad (25)$$

where $s(T)$ is a temperature scaling function that does not depend on f within a limited range of frequencies (see Appendix A8). If

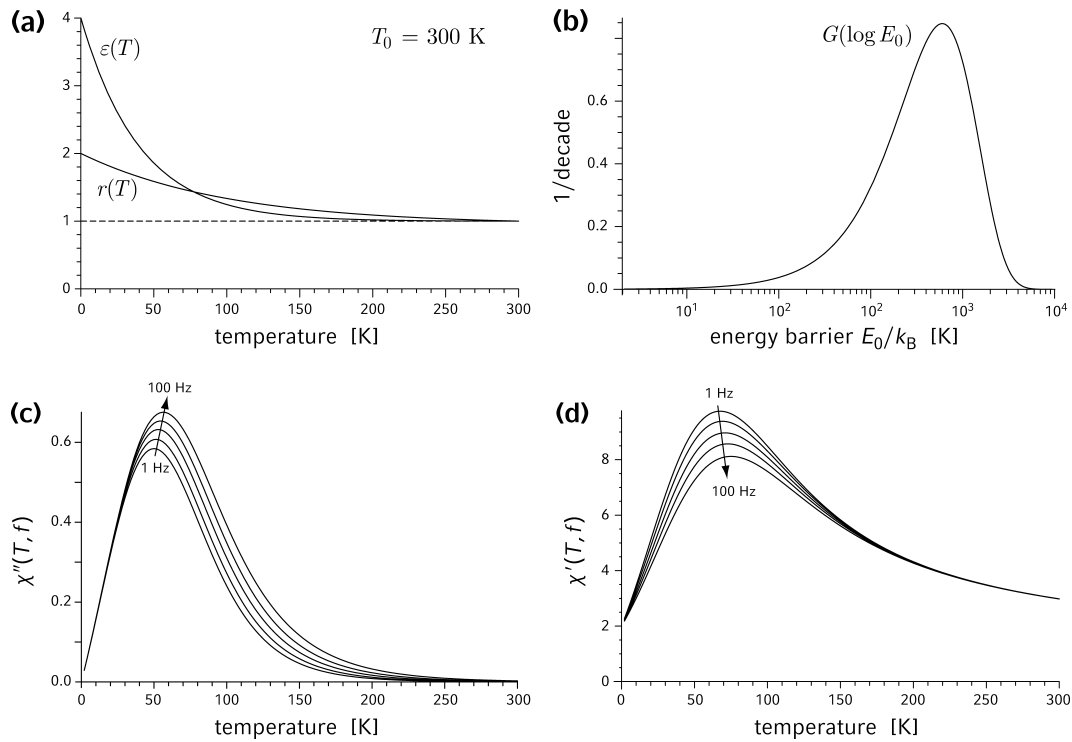


Figure 7. Numerical model of randomly oriented SW particles used throughout this paper to test the inversion of susceptibility measurements. (a) Temperature dependences $r(T)$ and $\varepsilon(T)$ and (b) energy barrier distribution $G(\log E_0)$ used to simulate error-free measurements of the imaginary (c) and real (d) susceptibility as a function of temperature for $f = 1, 3, 10, 30$ and 100 Hz. Other model parameters are $\tau_0 = 10^{-10}$ s and $h_0 = 0.01$.

the scaled temperatures T_{kj}^* are known, $s(T)$ can be calculated at discrete points using (24–25) to obtain

$$s(T_{kj}^*) = \frac{T_k}{T_{kj}^*} \frac{1}{(\lambda_j - 1)}. \quad (26)$$

Considering again the limit case $\lambda \rightarrow 1$, (25–26) are now used to substitute u in (15) and obtain a differential equation in $\varepsilon(T)$ that has the following solution:

$$\varepsilon(T) \approx \frac{T}{T_0} \exp \left[- \int_{T_0}^T \frac{du}{us(u)} \right], \quad (27)$$

with $\varepsilon(T_0) = 1$ (see Appendix A8). Eq. (27) is affected by a linearization error due to the assumption that $\lambda \rightarrow 1$. This error can be corrected through a recursive calculation of $\varepsilon(T)$ as explained in the following.

The first recursion step consists in calculating the scaled temperatures T_{kj}^* . Different methods can be implemented for this purpose. A method based on least-squares polynomial fits is shown in Fig. 8. The range of measured temperatures is first divided into intervals where the coordinates (T_k, q_{kj}) can be piecewise fitted using a second-order polynomial. A set of polynomials $Q_{ij}(T)$ that fit the temperature dependence of q_j in each temperature interval $[T_i, T_{i+1}]$ is then obtained for each frequency f_j . In each temperature interval, characterized by the average temperature $\bar{T}_i = (T_i + T_{i+1})/2$, a positive number S_i is found, such that the mean squared difference,

$$\sum_j \sum_{T_k \in [T_i, T_{i+1}]} \{Q_{ij}[(\lambda_j - 1)S_i T_k] - Q_{i1}(T_k)\}^2, \quad (28)$$

between the polynomials with scaled temperatures $(\lambda_j - 1)S_i T_k$ is minimized. In eq. (28), f_1 is taken as a reference frequency, and $\lambda_j = \ln(2\pi\tau_0 f_1) / \ln(2\pi\tau_0 f_j)$. Since $T_k = (\lambda_j - 1)S_i T_{kj}^*$, the solutions (\bar{T}_i, S_i) represent a first discretization $s_0(T_i)$ of the temperature

scaling function $s(T)$, which is then used to solve (27) and obtain a first estimate $\varepsilon_0(T)$ of ε . Now ε is replaced by $\varepsilon_0(T)$ in eq. (15), which is then solved numerically with respect to u . The solution $u_0(T, f)$ is substituted into (25) and the resulting equation is in turn solved with respect to $s(T)$. The solution $s_0^*(T)$ differs slightly from $s_0(T_i)$ because of the linearization error $\Delta s_0 = s_0^* - s_0$. If Δs_0 is positive (negative), the error of $\varepsilon_0(T)$ produces a temperature scaling function $s_0^*(T)$ that is too large (small). One can compensate for this error by adjusting $\varepsilon_0(T)$ so that Δs_0 is cancelled. This leads to the next recursion step, where $\varepsilon_1(T)$ is calculated using $s_1 = s_0 - \Delta s_0$ instead of s_0 . This approach provides a sequence $\varepsilon_n(T)$ of successive estimates of $\varepsilon(T)$, based on the sequential solution of (15), (25) and (27). The sequence ε_n eventually converges to a final estimate $\hat{\varepsilon}(T)$ that theoretically coincides with $\varepsilon(T)$ for error-free measurements and a correct choice of the other model parameters.

The method explained above has been tested using the numerical example of Fig. 7. The reconstructed $\varepsilon(T)$ is in good agreement with the original function used to calculate the forward model (Fig. 8c). Nevertheless, despite the perfect overlap of the functions $q_j(T_{kj}^*)$ (Fig. 8d), there is a small difference between $\hat{\varepsilon}(T)$ and $\varepsilon(T)$, especially as $T \rightarrow 0$. The difference arises from the amplification of numerical errors due to the fact that the limit of (27) for $T \rightarrow 0$ diverges if $s(T \rightarrow 0) < 1$ (see Appendix A8 for a detailed explanation). Therefore, incorrect estimates of $r(T)$, h_0 or τ_0 , as well as large measurement errors, might result in a diverging $\hat{\varepsilon}(T)$ for $T \rightarrow 0$.

A figure of merit for the reconstruction of $\varepsilon(T)$ is provided by the mean quadratic difference $\langle \delta q^2 \rangle$ between the functions $q_j(T_{kj}^*)$ for all measured frequencies. Since the T_{kj}^* are all different, numerical interpolations \tilde{q}_j of q_j must be used to calculate $\langle \delta q^2 \rangle$, which is then

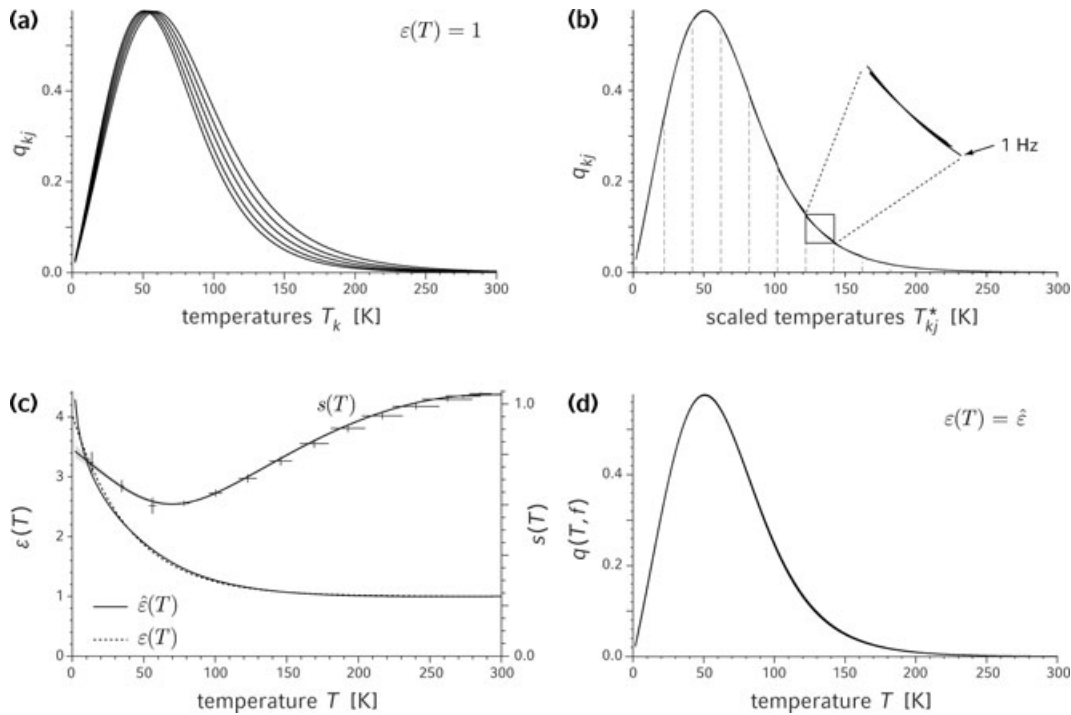


Figure 8. Reconstruction of $\varepsilon(T)$ from measurements $\chi''_{kj} = \chi''(T_k, f_j)$ of the imaginary susceptibility, obtained using exact values of $r(T)$ and h_0 . (a) The first step consists in replacing χ''_{kj} by q_{kj} obtained from (24). The amplitude of the scaled curves is now independent of f , unlike $\chi''(T, f)$ in Fig. 7c. (b) The measurement temperatures T_k are grouped into a number of intervals (dashed lines). In each interval, rescaled measurement temperatures T_k^* are calculated to obtain perfectly overlapping curves defined by the coordinates (T_k^*, q_{kj}) . The insert is an enlarged view of (T_k^*, q_{kj}) within one temperature interval. (c) Empirical estimates S_k of the scaling function used to calculate T_k^* in each temperature interval (crosses indicating the estimated errors) are extrapolated to a continuous scaling function $s(T)$ (solid line). The scaling function $s(T)$ is used to calculate an estimate $\hat{\varepsilon}(T)$ (solid line) of $\varepsilon(T)$ (dashed line). (d) A perfect overlap of the functions $q(T, f_j)$ calculated using $\hat{\varepsilon}(T)$ shows that the reconstructed $\varepsilon(T)$ is compatible with the measurements.

given by

$$\langle \delta q^2 \rangle = \sum_{k,j} [\tilde{q}_j(u_k) - q_1(T_k)]^2, \quad (29)$$

where u_k is the solution of (15) for $\varepsilon = \hat{\varepsilon}(T)$, $f = f_j$ and $T = T_k$. Very small values of $\langle \delta q^2 \rangle$ are obtained from error-free measurements and a correct guess of $r(T)$, h_0 and τ_0 , as shown for the synthetic example of Fig. 7. Small errors introduced by approximations of the forward model discussed in Section 3, and by the piecewise fit of $q_j(T_k)$ using second-order polynomials prevent $\langle \delta q^2 \rangle$ from being exactly zero in the synthetic example. In practice, measurement errors and incorrect choices of the other model parameters result in much larger values of $\langle \delta q^2 \rangle$.

A possible problem in reconstructing $\varepsilon(T)$ is given by the numerical instability of (27) if $s(T)$ does not tend to a number > 1 as $T \rightarrow 0$. In this case, small measurement errors, as well as possible intrinsic approximations of the SSR model, could become largely amplified in the calculation of $\varepsilon(T)$ at very low temperatures. To avoid dealing with instabilities of $\varepsilon(T \rightarrow 0)$ due to measurement errors, a stabilized version $\tilde{\varepsilon}(T)$ of $\hat{\varepsilon}(T)$ might be calculated by imposing $s(0) = 1$. Since $T_1 > 0$ in real measurements, this can be easily done by adding $(T = 0, S_0 = 1)$ to the solutions (\tilde{T}_i, S_i) of (28), and forcing the interpolated function $s(T)$ through the added point.

4.3 Reconstruction of $r(T)$

As discussed in Section 4.1, the relation between the real and the imaginary components of $\chi(T; f)$ is controlled mainly by $r(T)$.

Therefore, a correct guess of $r(T)$ can be tested by reconstructing $\chi'(T; f)$ from $\chi''(T; f)$ using eq. (19), and comparing the reconstructed in-phase susceptibility $\hat{\chi}'(T; f)$ with measurements of $\chi'(T; f)$. In addition to $\varepsilon(T)$, $r(T)$, h_0 and τ_0 , an estimate of b is also needed for this purpose. Following model,

$$\hat{\chi}'(T, f) = b\kappa(T) + \chi'_{sw}(T, f) + \frac{C_p}{T}, \quad (30)$$

describes the reconstructed in-phase susceptibility of samples containing a mixture of SP particles and paramagnetic minerals with a paramagnetic susceptibility C_p/T . If paramagnetic minerals are absent, as in many synthetic samples, $C_p = 0$. The interpretation of in-phase susceptibility measurements of rocks and sediments on the left-hand side of (30) is possible only if pseudo-SD or multidomain grains are absent. To ensure such condition, magnetic extraction should be used to remove large grains, prior to the measurement.

Since $\chi'_{sw}(T, f)$ and $\kappa(T)$ are calculated using (19) and (20), the right-hand side of (30) contains only two unknown parameters, b and C_p . Least-squares methods provide estimates of b and C_p that minimize the difference $\Delta\chi' = \hat{\chi}' - \chi'$ between reconstructed and measured in-phase susceptibility. The residual difference $\Delta\chi'$ obtained after optimizing b and C_p is mainly a function of $r(T)$.

In the following, a method is developed for estimating $r(T)$ through successive approximations $r_i(T)$ of $r(T)$, with $r_i(T_0) = 1$ and $k = 0, 1, 2, \dots$, whereby $\varepsilon(T)$, h_0 and τ_0 are assumed to be known. Let the error of each approximation $r_i(T)$ be specified by the function $\rho_i(T)$, such that $r = r_i(1 + \rho_i)$. If $r_i(T)$ is close to the exact solution, $|\rho_i| \ll 1$ and (19) can be linearized with respect to ρ . A further simplification is obtained if $|2h_0 r \ln w| < 0.6$, allowing one to ignore the dependence of the cosh terms on $r(T)$. Since χ'_{sw}

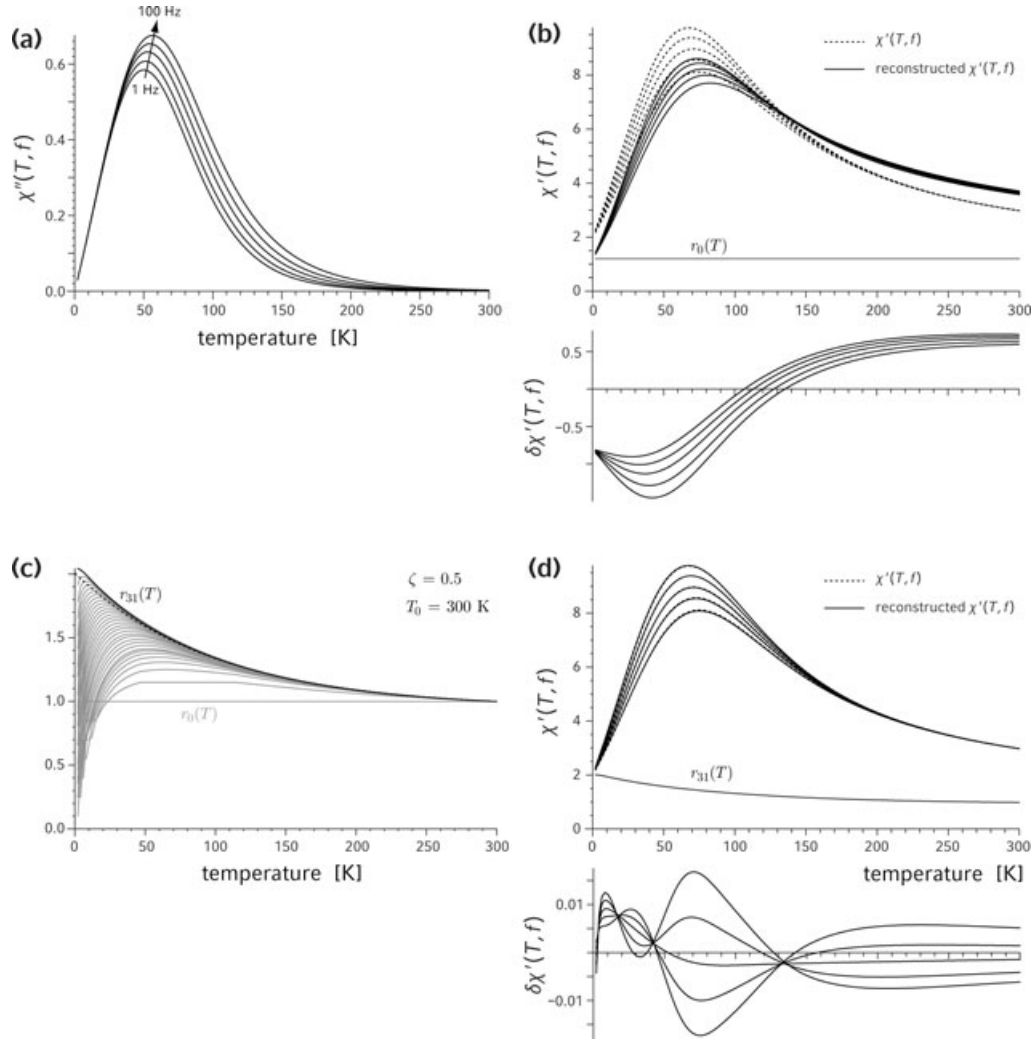


Figure 9. Reconstruction of $r(T)$ using exact values of $\varepsilon(T)$ and h_0 . (a) Simulated measurements of the imaginary susceptibility component $\chi''(T, f)$ at five different frequencies, as specified in Fig. 7. (b) Using an initial function $r_0(T) = 1$, the real component of the susceptibility is calculated from $\chi''(T, f)$ (solid lines). Simulated measurements of $\chi'(T, f)$ (dashed lines) are shown for comparison. The difference $\delta\chi'$ between measured and reconstructed susceptibility (shown below) is then used to calculate the successive estimate $r_1(T)$ of $r(T)$. (c) The first 31 estimates of $r(T)$ (solid lines) obtained recursively as explained in (b). The exact $r(T)$ is shown for comparison (dashed line). (d) $\chi'(T, f)$ reconstructed from $\chi''(T, f)$ using $r_{31}(T)$ (solid lines) coincides precisely with the simulated measurements (dashed lines). The small residual model misfit $\delta\chi'$ is shown below.

is practically zero for $-\ln w > 20$, the simplification is valid for $h_0 < 0.015/r$. Since $h_i = h_0 r$, this limit coincides with the validity range of the weak interaction model of Shcherbakov & Fabian (2005) discussed in Section 2.3.

After some algebraic manipulations (see Appendix A9), the following linear differential equation in $\rho_i(T)$ is obtained from (19):

$$\frac{T\chi'_{\text{sw},i}(T, f) \partial \rho_i(T)}{r_i(T)\varepsilon(T)} \approx -\frac{\partial}{\partial T} \frac{T\Delta\chi'_{\text{sw},i}(T, f)}{r_i(T)\varepsilon(T)}, \quad (31)$$

where $\Delta\chi'_{\text{sw},i} = \chi'_{\text{sw}}(r_i) - \chi'_{\text{sw}}(r)$ is the difference between χ'_{sw} s estimated using $r_i(T)$ and $r(T)$, respectively. Since $\chi'_{\text{sw}}(r)$ is not directly measurable, (30) is used to obtain the explicit expression $\Delta\chi'_{\text{sw},i} = \hat{\chi}'_i - \chi' + b\kappa\rho_i$, which is based on the fact that κ in (20) is approximately proportional to r . The differential eq. (31) is not easily integrable, because $\Delta\chi'_{\text{sw},i}$ contains the unknown ρ_i . Therefore, a further simplification is introduced by assuming $\chi'_{\text{sw}} \gg \chi_{\text{ns}}$, so that $\Delta\chi'_{\text{sw},i} \approx \hat{\chi}'_i - \chi'$. This assumption is generally valid throughout the range of unblocking temperatures of the particles (Fig. 4). If $\Delta\chi'_{\text{sw},i} \approx \hat{\chi}'_i - \chi'$, (31) is easily integrated over T ,

obtaining

$$\rho_i(T) \approx \int_{T_0}^T \frac{r_i(u)\varepsilon(u)}{u\chi'(u)} \frac{\partial}{\partial u} \frac{u[\chi'(u) - \hat{\chi}'(u, r_i)]}{r_i(u)\varepsilon(u)}, \quad (32)$$

with $\rho_0(T_0) = 0$ and $\hat{\chi}'(T, r_i)$ defined in (30). This result is now used to calculate a better estimate of $r(T)$, according to the following recursion formula:

$$\{b_i, C_{p,i}\} = \{b, C_p\} \left| \sum_{T_k, f_j} \left[\chi'(T_k, f_j) - b_{\text{ns}}\kappa(T_k, r_i) - \chi'_{\text{sw}}(T_k, f_j, r_i) - \frac{C_p}{T_k} \right]^2 \right| \stackrel{!}{=} \min \quad (33)$$

$$r_{i+1}(T) = r_i(T) + \zeta r_i(T) \times \int_{T_0}^T \frac{r_i(u)\varepsilon(u)}{u\chi'(u)} \frac{\partial}{\partial u} \frac{u[\chi'(u) - \hat{\chi}'(u, r_i, b_{\text{ns},i}, C_{p,i})]}{r_i(u)\varepsilon(u)} du,$$

where $0 < \zeta \leq 1$ is a damping factor used to stabilize the convergence of $r_i(T)$ toward an asymptotic value $\hat{r}(T)$. Numerical differentiation and integration are used to calculate the second row of (33).

The recursive formula (33) is based on assumptions discussed above, which might not be strictly valid in certain temperature ranges. However, the only requirement for (33) is to yield a series of $r_i(T)$ that converge to the exact solution. Convergence is ensured if the approximated solution for $\rho_i(T)$ given in (32) has the same sign as the exact solution of (31) for all measured temperatures. This relaxed condition allows for a reconstruction of $r(T)$ for typical sets of SP particles.

A reconstruction of $r(T)$ based on the numerical example of Fig. 7 is shown in Fig. 9, whereby $r_0(T) = 1$, and correct values of $\varepsilon(T)$, h_0 and τ_0 have been chosen as starting parameters. The in-phase susceptibility calculated from $\chi''(T; f)$ using the initial model $r_0(T)$ is clearly at odds with the simulated measurements. After 32 iterations based on (33) with $\zeta = 0.5$, convergence to a final estimate $\hat{r}(T)$ of $r(T)$ was obtained within <2 per cent over the entire range of temperatures. The in-phase susceptibility calculated from $\chi''(T; f)$ using $\hat{r}(T)$ is in excellent agreement with the simulated measurements, with a maximum difference of 0.1 per cent between χ' and $\hat{\chi}'$. Since the synthetic data are free of measurement errors, the residual difference is related to approximations in numerical integration and differentiation.

A figure of merit of $\hat{r}(T)$ is given by the standard deviation of the squared differences between χ' and $\hat{\chi}'$ calculated for all temperatures and frequencies:

$$\langle \delta\chi'^2 \rangle = \sum_{k,j} [\hat{\chi}'(T_k, f_j) - \chi'(T_k, f_j)]^2. \quad (34)$$

A minimum of $\langle \delta\chi'^2 \rangle$ is obtained asymptotically after a number of iterations. Extended testing of the algorithm on numerical and real samples has shown that $\zeta = 0.5$ and 20–60 iterations are sufficient to minimize $\langle \delta\chi'^2 \rangle$ in most cases. Convergence is more difficult when $r(T)$ or $\varepsilon(T)$ are strong functions of the temperature, or if h_0 approaches the upper validity range of the interaction model used in this paper. Those cases could still be solved starting from $r_0(T) = 1$ and using $\zeta = 0.05$ – 0.2 to avoid oscillatory instabilities.

In the ideal case of error-free measurements, $\langle \delta\chi'^2 \rangle \rightarrow 0$ is obtained when correct estimates of $\varepsilon(T)$, h_0 and τ_0 are used. In practice, however, $\langle \delta\chi'^2 \rangle$ does not decrease below a minimum value $\langle \delta\chi'^2 \rangle_{\min} > 0$. It is interesting to discuss $\langle \delta\chi'^2 \rangle_{\min}$ obtained using incorrect models of $\varepsilon(T)$, h_0 or τ_0 , since this is the typical case encountered while $r(T)$ is reconstructed. The initial forward model is characterized by $\delta\chi' = \hat{\chi}' - \chi'$ being both temperature- and frequency dependent (Fig. 9b). After an optimal estimate of $r(T)$ is found, the temperature dependence of $\delta\chi'$ is suppressed on average, but a residual dependence of $\delta\chi'$ on the frequency remains (Fig. 9d). The frequency dependence of $\delta\chi'$ is much larger than the measurement errors as long as incorrect estimates of the other model parameters are used to calculate $r(T)$. Therefore, $\langle \delta\chi'^2 \rangle_{\min}$ depends on the choice of $\varepsilon(T)$, h_0 and τ_0 , and it is possible to combine the inversion methods described in Sections 4.2 and 4.3 to obtain a solution for all model parameters, as discussed in the following section.

4.4 Combined inversion solution for all model parameters

The calculation of $r(T)$ and $\varepsilon(T)$ discussed previously is based on the assumption that one model parameter at the time is unknown. The next step consists in combining the reconstruction of $r(T)$ and $\varepsilon(T)$ for given values of the other two parameters h_0 and τ_0 . Using the same approach developed in Sections 4.2—and 4.3, $\varepsilon(T)$ and $r(T)$ can be calculated starting from initial estimates $\varepsilon_0(T)$ and

$r_0(T)$, whereby the solution of the inverse problem is applied alternatively to the two parameters. Accordingly, $\varepsilon_1(T)$ is the solution obtained with $r = r_0$ and h_0, τ_0 , which is then used to calculate $r_1(T)$. The procedure is reiterated to obtain new estimates ε_2 and r_2 . The series of solutions $\varepsilon_i(T)$ and $r_i(T)$ eventually converges to asymptotic functions $\hat{\varepsilon}(T)$ and $\hat{r}(T)$ that represent the final solution of the inverse problem for given values of h_0 and τ_0 . Convergence is ensured if the initial model functions were close enough to the correct solution. It will be shown later that convergence is generally robust, and simple initial guesses such as $r_0 = \varepsilon_0 = 1$ are sufficient. The solution $\hat{\varepsilon}(T)$ and $\hat{r}(T)$ of the inverse model is correct only if the figures of merit $\langle \delta q^2 \rangle$ and $\langle \delta\chi'^2 \rangle$ obtained from the last iteration have reached minimum values that correspond to the measurement errors. Depending on the choice of h_0 and τ_0 , differences will persist between the measurements and the forward model calculated using $\hat{\varepsilon}(T)$ and $\hat{r}(T)$ until a correct guess for h_0 and τ_0 is found.

The final step consists in finding the appropriate values of h_0 and τ_0 that minimize $\langle \delta q^2 \rangle$ and $\langle \delta\chi'^2 \rangle$. Well-defined constraints exist for both parameters. The weak interaction model discussed in Section 2.3 is valid only if $0 \leq h_0 \leq 0.015$: solutions for h_0 that fall out of this range are probably not correct and should be discarded. Empirical estimates of τ_0 are usually obtained by combining experiments that cover different timescales, such as Mössbauer spectroscopy ($\tau \approx 10^{-8}$ s) and susceptibility or magnetic relaxation measurements ($\tau \approx 10^{-2}$ – 10^2 s). Pre-exponential factors reported in the literature for SD particles vary with size and composition between 10^{-12} s for ferritin (Dickson *et al.* 1993) and 4×10^{-9} s for ferromagnetic particles in the SP–SD range (Moskowitz *et al.* 1997; Wernsdorfer 1997a; Egli & Lowrie 2002). Unphysical values $< 10^{-13}$ s are obtained if magnetostatic interactions are not adequately accounted for (Dormann *et al.* 1997; Shcherbakov & Fabian 2005). Therefore, $10^{-13} \leq \tau_0(\text{s}) \leq 10^{-8}$ represents the maximum range of realistic pre-exponential factors to consider.

The limited range of possible values for h_0 and τ_0 allows one to solve the inverse problem by exploring the validity ranges of $\log \tau_0$ and h_0 in uniform steps. The parameter pair (h_0, τ_0) that produces a forward model closest to the measurements corresponds to a global minimum of both $\langle \delta q^2 \rangle$ and $\langle \delta\chi'^2 \rangle$ and represents the full solution of the inverse problem. A protocol for the full inversion of susceptibility measurements based on this concept can be summarized to the following steps:

- (1) Measure $\chi(T; f)$ over the widest possible temperature range using a set of frequencies that typically extends over two decades (e.g. 1, 10 and 100 Hz). If measurements are performed over more than three frequency decades, the frequency dependence of $\chi(T; f)$ is no longer approximated by a linear function, invalidating (25). Therefore, the inversion of such measurements should be performed after splitting the measured frequencies in groups that are analysed separately. Measurements over small temperature steps at few frequencies are therefore best suited for inversion, easing the choice of the frequency range for which the instrument is most sensitive. A range of temperatures sufficient to block/unblock all particles is of advantage but not necessary.

- (2) Choose the initial model parameters. If composition and size of the magnetic particles are fully unknown, $\tau_0 = 10^{-10}$ s, $h_0 = 0$ and $r_0(T) = \varepsilon_0(T) = 1$ is a good initial guess. Better initial parameters can be chosen if additional information is available. Choose a reference temperature T_0 within the range of measured temperatures. Avoid setting T_0 equal or close to 0 K, since large uncertainties occur in the reconstruction of $r(T)$ and $\varepsilon(T)$ for $T \rightarrow 0$.

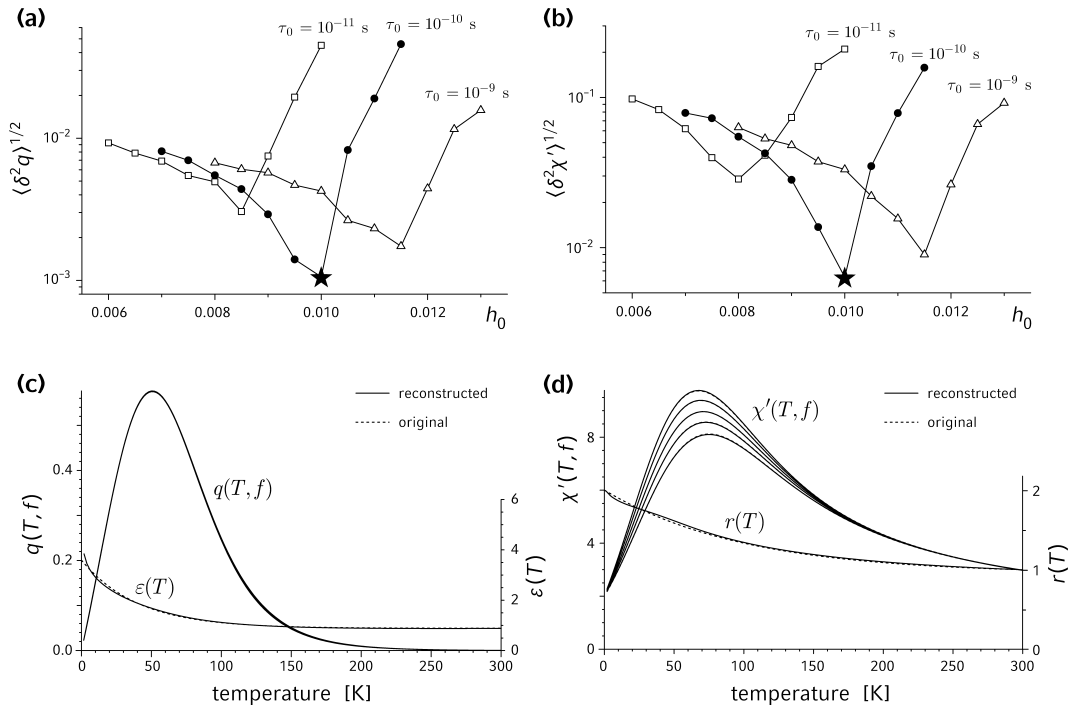


Figure 10. (a) and (b) Figures of merit for the inversion of the simulated susceptibility measurements of Fig. 7, obtained for a series of τ_0 and h_0 values. In both cases, best results are achieved using $\tau_0 = 10^{-10}$ s and $h_0 = 0.01$ (star), which coincide with the parameters used to calculate the simulated measurements. (c) and (d) Reconstruction of $\varepsilon(T)$ and $r(T)$ for the final model corresponding to $\tau_0 = 10^{-10}$ s and $h_0 = 0.1$.

(3) Calculate a first estimate $\hat{\varepsilon}(T)$ of $\varepsilon(T)$ using the method described in Section 4.2 and fixed parameters τ_0 , h_0 and $r_0(T)$. Limit the temperature range considered for reconstructing $\varepsilon(T)$ to measurements of $\chi''(T; f)$ that are well above the noise level. Set $\varepsilon_0(T) = \hat{\varepsilon}(T)$ before proceeding with step 4.

(4) Obtain a first estimate $\hat{r}(T)$ of $r(T)$ using the method described in Section 4.3 and fixed parameters τ_0 , h_0 and $\varepsilon_1(T)$. Use a sufficient number of iterations to obtain a convergent result and verify that $\delta\chi' = \hat{\chi}' - \chi'$ after the last iteration step does not show a systematic dependence on T (e.g. $\delta\chi'$ should look like Fig. 9d, and not like Fig. 9b). This condition is always verified after a sufficient number of iterations. Set $r_0(T) = \hat{r}(T)$ before proceeding with step 5.

(5) Repeat steps 3 and 4 until a stable solution for $r(T)$ and $\varepsilon(T)$ is obtained. The inverse problem for the parameter pair (τ_0, h_0) is now solved. A figure of merit of the resulting susceptibility model is given by $\langle \delta q^2 \rangle$ and $\langle \delta \chi^2 \rangle$.

(6) Repeat steps 2–5 for various parameter pairs (τ_0, h_0) obtained by exploring the validity ranges of $\log \tau_0$ and h_0 in uniform steps. Suggested initial steps are one order of magnitude for τ_0 (e.g. 10^{-12} , 10^{-11} , 10^{-10} s) and 0.005 for h_0 . Refine the steps if necessary.

(7) There should exist one pair of parameters $(\hat{\tau}_0, \hat{h}_0)$ for which both $\langle \delta q^2 \rangle$ and $\langle \delta \chi^2 \rangle$ are absolute minima. These parameters, together with the corresponding inverse problem solutions $\hat{r}(T)$ and $\hat{\varepsilon}(T)$, represents the final result of susceptibility inversion.

An example of inverse problem solution based on this protocol has been calculated for the numerical model of Fig. 7. Combinations of τ_0 and h_0 given by $\tau_0 = 10^{-11}$, 10^{-10} and 10^{-9} s and $0.006 \leq h_0 \leq 0.013$ in steps of 5×10^{-4} have been used (Figs 10–13). A solution that minimizes both $\langle \delta q^2 \rangle$ and $\langle \delta \chi^2 \rangle$ is obtained only

when τ_0 and h_0 coincide with the model parameters used to generate the simulated measurements (Figs 10a and b). In this example, the inversion problem has a single solution that coincides with the model parameters used to calculate the simulated measurements. If h_0 is arbitrarily set to zero, the minimization of $\langle \delta q^2 \rangle$ and $\langle \delta \chi^2 \rangle$ forces τ_0 to unrealistically small values, in concert with the conclusions of Shcherbakov & Fabian (2005). Incorrect choices of h_0 and of τ_0 produce a clear mismatch between the forward model and the synthetic data (Figs 11 and 12).

When error-free measurements are analysed, $\langle \delta q^2 \rangle \simeq 0$ and $\langle \delta \chi^2 \rangle \simeq 0$ are obtained for one and the same combination of model parameters, provided that the forward model discussed in Section 3 is correct. If different values of τ_0 and h_0 are needed to minimize $\langle \delta q^2 \rangle$ and $\langle \delta \chi^2 \rangle$, at least one of the assumptions underlying the forward model is wrong, as discussed in Section 5. However, small differences between the values of τ_0 and h_0 that minimize $\langle \delta q^2 \rangle$ and $\langle \delta \chi^2 \rangle$ could arise from measurement errors or from acceptable approximations of the forward model. In this case, a meaningful solution of the inverse problem might be found by defining a single figure of merit Φ . Since $\langle \delta q^2 \rangle$ and $\langle \delta \chi^2 \rangle$ differ typically by at least one order of magnitude (Fig. 10), the product $\Phi = \langle \delta q^2 \rangle \langle \delta \chi^2 \rangle$ is a choice that weights equally the real and the imaginary component of susceptibility.

4.5 Reconstruction of the energy barrier distribution

Once the model parameters $r(T)$, $\varepsilon(T)$, τ_0 and h_0 have been determined, it is possible to calculate the EBD $G(E_0)$. As discussed previously, a logarithmic scale is often more appropriate to represent EBD extending over several orders of magnitude. An estimate of the distribution function for $\log E_0$ is obtained from (13) using

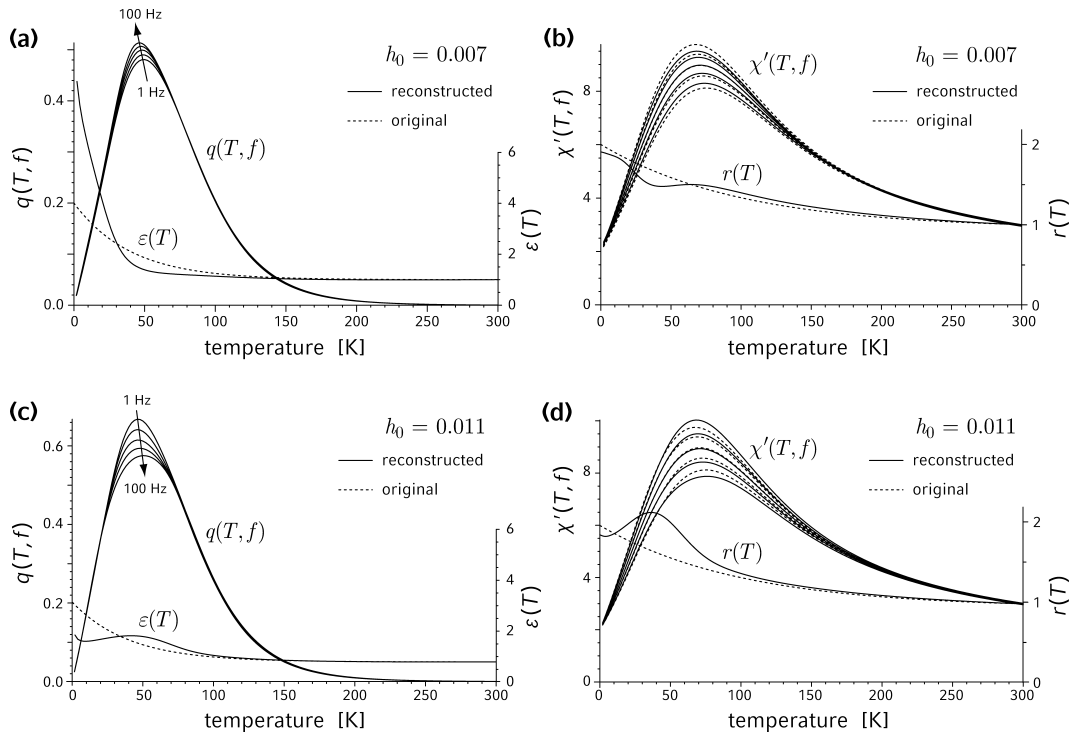


Figure 11. Effects of the interaction field parameter h_0 on the calculation of $\varepsilon(T)$ and $r(T)$. The estimated parameters $\hat{\varepsilon}(T)$ and $\hat{r}(T)$ have been reconstructed using $\tau_0 = 10^{-10}$ s and (a and b) $h_0 = 0.007$, (c and d) $h_0 = 0.011$, instead of the correct value $h_0 = 0.01$. Left-hand panel: the functions $q(T, f_j)$ and $\hat{\varepsilon}(T)$ (solid lines); $\varepsilon(T)$ (dashed line) is shown for comparison. Right-hand panel: reconstructed $\hat{\chi}'(T, f)$ and $\hat{r}(T)$ (solid lines); simulated measurements of $\chi'(T, f)$ and $r(T)$ are shown for comparison (dashed lines).

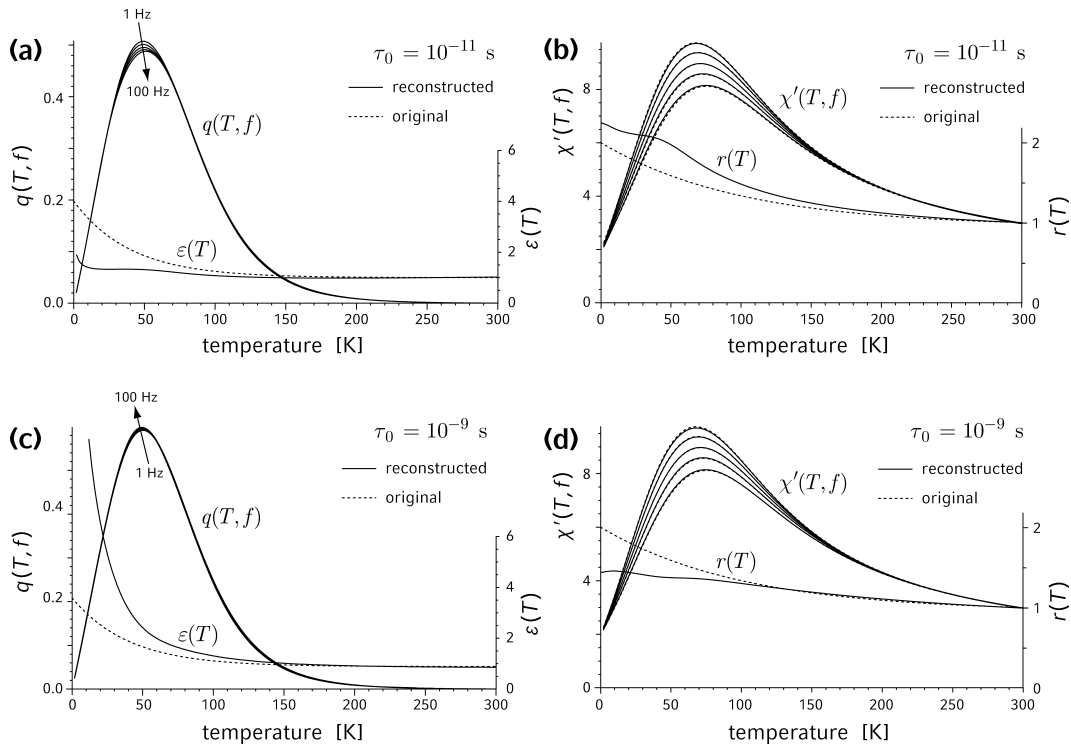


Figure 12. Effects of the pre-exponential factor τ_0 on the calculation of $\varepsilon(T)$ and $r(T)$. The estimated parameters $\hat{\varepsilon}(T)$ and $\hat{r}(T)$ have been reconstructed using $h_0 = 0.1$ and (a and b) $\tau_0 = 10^{-11}$ s, (c and d) $\tau_0 = 10^{-9}$ s, instead of the correct value $\tau_0 = 10^{-10}$ s. Left-hand panel: the functions $q(T, f_j)$ and $\hat{\varepsilon}(T)$ (solid lines); $\varepsilon(T)$ (dashed line) is shown for comparison. Right-hand panel: reconstructed $\hat{\chi}'(T, f)$ and $\hat{r}(T)$ (solid lines); simulated measurements of $\chi'(T, f)$ and $r(T)$ are shown for comparison (dashed lines).

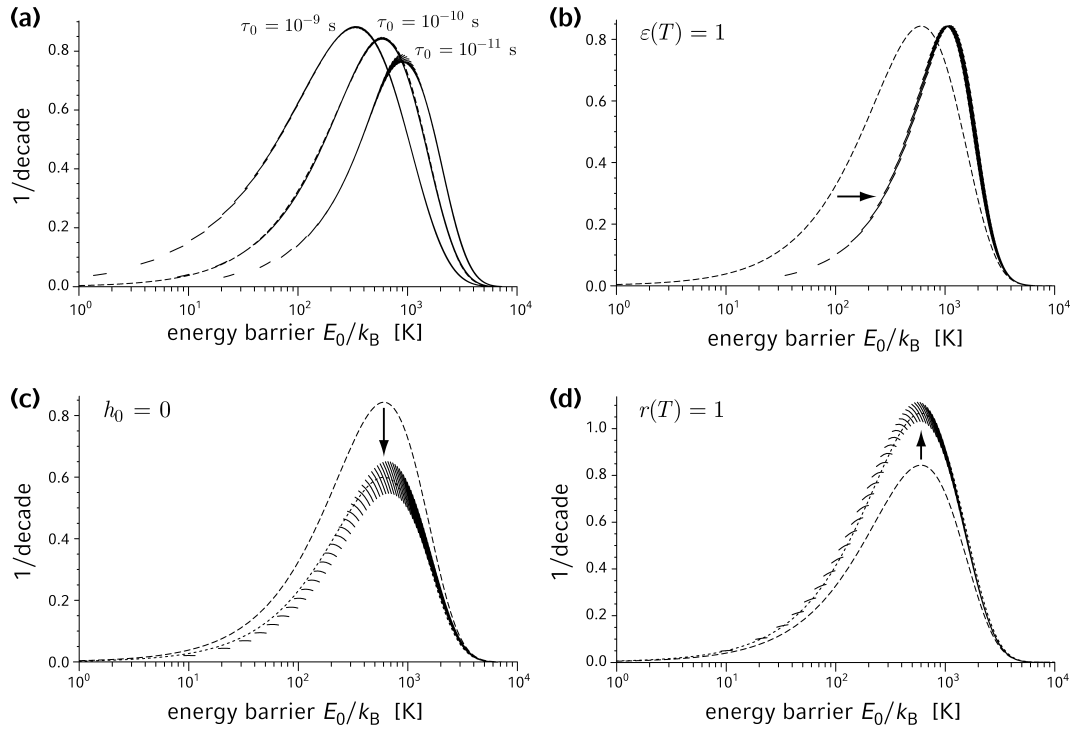


Figure 13. Reconstructed energy barrier distributions (EBD) $\hat{G}(\log E_0)$, represented by solid line segments corresponding to measurements performed at the same temperature. The EBD used to calculate the simulated measurements, $G(\log E_0)$, is shown for comparison (dashed line). (a) EBD obtained for three different values of τ_0 and a combination of model parameters that minimize $\langle \delta q^2 \rangle$ and $\langle \delta \chi^2 \rangle$ for each value. (b) EBD reconstruction obtained using $\varepsilon(T) = 1$. The other model parameters are identical to those used for the forward model. (c) EBD reconstruction obtained using $h_0 = 0$. The other model parameters are identical to those used for the forward model. The wrong choice of h_0 affect the amplitude of \hat{G} (arrow) but has little influence on the shape of the distribution, as shown by rescaling G (dotted line) to fit \hat{G} . (d) EBD reconstruction obtained using $r(T) = 1$. The other model parameters are identical to those used for the forward model. The amplitude of \hat{G} is affected by a wrong choice of $r(T)$ (arrow), but the shape of the distribution remains unchanged, as shown by rescaling G (dotted line) to fit \hat{G} .

the transformation role for distribution variables:

$$\hat{G}(\log E_0) = \frac{2 \ln 10}{\pi \xi_b r(T) J[2h_0 r(T) \ln w]} \chi''(T, f), \quad (35)$$

$$T/\varepsilon(T) = -E_0/(k_B \ln w).$$

The EBD can be plotted directly from measurements of $\chi''(T; f)$ using the coordinates

$$E_{0,k,j} = -k_B T_k \ln(2\pi\tau_0 f_j)/\varepsilon(T_k),$$

$$\hat{G}_{k,j} = \frac{2 \ln 10}{\pi \xi_b r(T_k) J[2h_0 r(T_k) \ln(2\pi\tau_0 f_j)]} \chi''(T_k; f_j). \quad (36)$$

If correct estimates of $r(T)$, $\varepsilon(T)$, τ_0 and h_0 are used, all points specified by (36) collapse on a single, smooth line representing the EBD.

Examples of energy barrier reconstruction based on the numerical model of Fig. 7 are shown in Fig. 13. The representation of Shcherbakov & Fabian (2005) has been used, where all points corresponding to measurements performed at the same temperature are connected by a line (isothermal lines). This representation has the advantage of clearly showing eventual incoherencies of the inversion method, since a perfect overlap of the isothermal lines is obtained only if all model parameters and the underlying assumptions of the forward model are correct (Fig. 13a).

Incorrect estimates of τ_0 affect the reconstruction of $\varepsilon(T)$, which in turn shifts the median of \hat{G} toward lower or higher energy barriers (Figs 13a and b). This shows the importance of avoiding arbitrary choices of τ_0 . On the other hand, $r(T)$ and h_0 influence the am-

plitude of \hat{G} , but not its shape, making energy barrier calculations relatively insensitive to the latter two parameters. This result is expected for h_0 , since it follows directly from the assumptions that weak magnetostatic interactions do not alter the energy barrier significantly.

4.6 SUSINVER code

The inversion method discussed in 4.2–4.5 has been implemented in the package SUSINVER running on Mathematica[®] 6.0 and later versions. SUSINVER provides a set of built-in Mathematica[®] functions for the calculation of the forward model, the inversion of susceptibility measurements and the graphical representation of $r(T)$, $\varepsilon(T)$ and $G(E_0)$. The forward models of Figs 4–7, as well as the inversion results of Figs 8–13, have been calculated using SUSINVER, which also provided most of the graphics shown in these figures. The graphical interface allows the user to check the inversion results and optimize parameters such as the number of iterations and the choice of temperature intervals for calculating $\varepsilon(T)$. SUSINVER is freely available on request from the author, together with solved examples and instructions for using the built-in functions.

5 INTERPRETATION AND LIMITS OF SUSCEPTIBILITY INVERSION

The limits of the susceptibility inversion method discussed in Section 4 are related to the assumptions underlying the forward

model, namely: (1) uniaxial anisotropy; (2) validity of the Néel–Brown relaxation model (i.e. eq. 3) and (3) the temperature dependences of m and H_K are independent of the particle's volume (Fig. 2d), and 4) the particle distribution in space is completely random (Fig. 1h). The implications of these assumptions will be discussed here, with particular emphasis on the interpretation of the inversion results.

5.1 Non-uniaxial anisotropy

The forward model describing the susceptibility of SP particles with non-uniaxial anisotropy has never been solved explicitly. Superparamagnetic relaxation calculations for mixed uniaxial and cubic anisotropies show that multiple relaxation rates exist between different equilibrium states of the same particle (Newell 2006a,b). The practical consequence for susceptibility measurements is that a single particle might be characterized by multiple blocking conditions. The most obvious effect is that identical particles with mixed anisotropy behave similarly to a set of uniaxial particles with different magnetic moments and energy barriers. Given this equivalence between one particle with mixed anisotropy and an appropriate set of fictive uniaxial particles, one would expect the forward model discussed in Section 3 to be still valid, as long as the EBD is not converted into a volume distribution. However, thermally activated transitions between different equilibrium configurations of the same particle are not independent from each other, as they would be in an equivalent model with multiple uniaxial particles. The lack of independence between different transitions could give rise to unexpected effects that might invalidate some aspects of the forward model discussed in Section 3. The case of cubic and mixed anisotropies will be discussed in detail in a follow-up paper.

5.2 Departures from the Néel–Brown relaxation model

As discussed in Dormann *et al.* (1997), the Néel–Brown relaxation model applies to non-interacting magnetic particles whose moment reverses by coherent rotation. This reversing mode has been verified experimentally for $T > 1$ K by direct relaxation time measurements of single Co nanoparticles with a diameter of 25 nm in a field slightly smaller than the switching field (Wernsdorfer *et al.* 1997a). Measurements on larger nanoparticles suggest that the magnetic moment reverses by a nucleation process. In such cases, best fit to the experimental data is obtained when the relaxation time constant $\tau = \tau_0 e^{\beta}$ is replaced by $\tau = \tau'_0 \exp(\beta^p)$, where p is a positive exponent (Wernsdorfer *et al.* 1995), giving rise to a so-called stretched exponential law for the relaxation time. A stretched exponential law seems also necessary to explain the same type of measurements on maghemite (Lederman *et al.* 1994) and the aging effect due to oxidation of Ni nanowires (Wernsdorfer *et al.* 1997b). These observations led to the suggestion that a stretched exponential relaxation law would apply to ferri- and antiferromagnetic particles, whereas the Néel–Brown law would be strictly valid only for ferromagnetic particles. This has profound implications in the interpretation of geologic materials, where remanence carriers are usually ferrimagnetic particles with various degrees of low-temperature oxidation. However, it should be noted that relaxation time experiments on single nanoparticles have been all performed in a strong field, and that deviations from the Néel–Brown relaxation model might not necessarily persist at low fields or in a zero field, such as with susceptibility measurements or during the acquisition of a thermoremanent magnetization in the Earth magnetic field. Measurements of a single

maghemite particle indeed show an increasingly better agreement with the Néel–Brown law as the field is decreased.

The effect of a stretched exponential relaxation law on the forward susceptibility model is investigated in the following by generalizing Néel's solution of the kinetic equation of isolated uniaxial particles to the case of a general relaxation law with transition rate $f(\beta)$ over the normalized energy barrier β . The Néel–Brown relaxation model is given by $f^{-1}(\beta) = \tau_0 e^{\beta}$, whereas a stretched exponential model is described by $f^{-1}(\beta) = \tau'_0 \exp(\beta^p)$ with $p > 0$. Using Néel's (1949) approach to the solution of the kinetic equation based on a generic transition rate $f(\beta)$, the switching susceptibility of isolated particles is given by

$$\chi_{sw} = \chi_0 \frac{f'(\beta)\beta}{f(\beta) + i\omega}. \quad (37)$$

The classic Néel solution (2) follows from $f^{-1}(\beta) = \tau_0 e^{\beta}$; on the other hand, the stretched exponential relaxation law gives

$$\chi_{sw} = \chi_0 \frac{p\beta^p}{1 + i\tau_0 \omega \exp(\beta^p)}. \quad (38)$$

Two examples for $p = 0.8$ and $p = 1.2$ are shown in Fig. 14. The blocking condition is given by $\beta_0 = -\ln^{1/p}(\tau_0 \omega)$, instead of

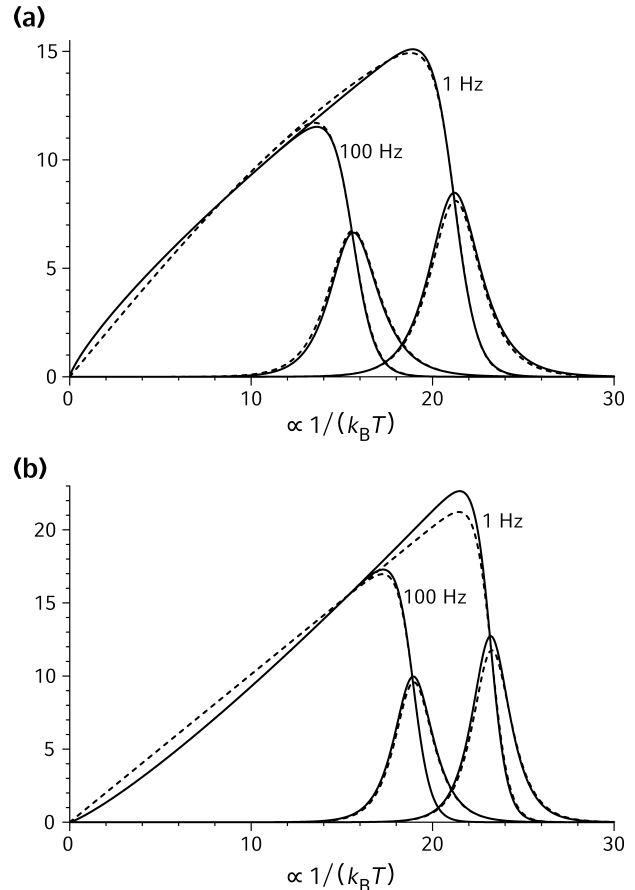


Figure 14. Switching susceptibility models of random assemblages of non-interacting particles with a stretched exponential relaxation law (solid lines), and best least-squares fit obtained using a Néel–Brown relaxation law (dashed line). (a) Real and imaginary part of χ_{sw} for $p = 0.8$, $E/k_B = 0.465$, $\tau_0 = 10^{-10}$ s and $\nu = 1100$ Hz. Best approximation using eq. (2) is obtained with $E/k_B = 1.23$, $h_i = 0.0155$ and $\tau_0 = 5.2 \times 10^{-9}$. (b) Real and imaginary part of χ_{sw} for $p = 1.2$, $E/k_B = 1.82$, $\tau_0 = 10^{-10}$ s and $\nu = 1100$ Hz. Best approximation using eq. (2) is obtained with $E/k_B = 0.936$, $h_i = 0$ and $\tau_0 = 2.67 \times 10^{-12}$ s.

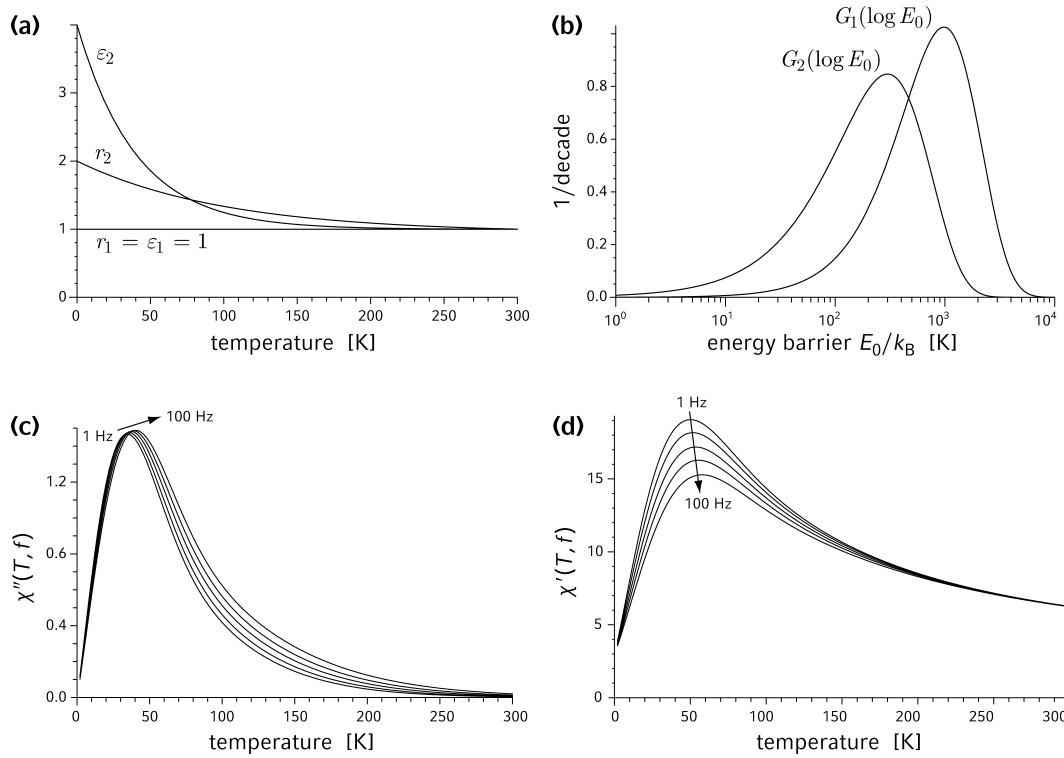


Figure 15. Numerical model of randomly oriented SW particles used to test the effect of a correlation between model parameters on the inversion of susceptibility data. The model consists in a mixture of two independent groups of particles characterized by (a) temperature dependences $r_1(T)$, $\epsilon_1(T)$ and $r_2(T)$, $\epsilon_2(T)$ respectively, (b) energy barrier distributions $G_1(\log E_0)$ and $G_2(\log E_0)$ and interaction field constants $h_0 = 0$ and $h_0 = 0.006$. The pre-exponential factor is $\tau_0 = 10^{-10}$ s, and no interactions are assumed to occur between the groups. The simulated susceptibility measurements of a sample containing these two groups of particles are shown in (c) and (d) for $f = 1, 3, 10, 30$ and 100 Hz.

$\beta_0 = -\ln(\tau_0\omega)$ as for the Néel–Brown relaxation model, producing a different frequency dependence. An additional effect of the stretched exponential relaxation law is the modification of the linear dependence of $\text{Re}\chi_{\text{sw}}$ on $\beta < \beta_0$. If $p < 1$, this effect is qualitatively similar to that produced by interactions in systems of randomly oriented particles. The temperature and frequency dependence of χ , calculated using a stretched exponential relaxation, is intrinsically different from the SSR forward model discussed in Section 3. However, forward SSR models with appropriate values of τ_0 and h_1 can produce a relatively good fit to the data if p is close to unit. This is especially true for $p < 1$, where a fictive interaction field approximates $\text{Re}\chi_{\text{sw}}$ for $\beta < \beta_0$. Nevertheless, forward susceptibility models calculated using $p = 0.8$ and 1.2 are clearly incompatible with the SSR model (Fig. 14). Therefore, a stretched exponential relaxation law is expected to produce a significant misfit between any SSR forward model and the measured data, allowing a clear identification of such cases.

5.3 Mixtures

An important assumption underlying the susceptibility inversion method presented here is based on the independence of the model parameters. This independence is necessary to solve the inversion problem, but one can easily imagine cases where a correlation exist between the volume of the particles, their temperature dependence and their arrangement in space (e.g. Figs 2e and i). For example, the magnetic anisotropy of small nanoparticles is affected by a surface contribution. The temperature dependence of surface anisotropy is not well understood; however, experiments on thin films show clear

differences with respect to volume anisotropy (André *et al.* 1995). Since the surface of a particle scales as $V^{2/3}$, smaller particles have a larger surface anisotropy contribution, and the temperature dependence of m and H_K might therefore depend on V . The spatial distribution of particles might also depend on their volume. If the particles are grown in a heterogeneous medium, such as a soil, different growing conditions in different parts of the sample could lead to the formation of particle aggregates characterized by different grain size distributions. In such cases, the distribution of interaction field and particle volumes could be different in each aggregate.

To understand the effect of correlations between model parameters, consider the simplest possible case given by a mixture of two isolated groups of SP particles. Each group is characterized by different magnetic parameters summarized in Fig. 15. The first group of particles has larger energy barriers, temperature-independent m and H_K and no magnetostatic interactions ($h_0 = 0$). The second group is composed of interacting particles ($h_0 = 0.006$) characterized by strong temperature dependence of m and H_K and smaller energy barriers. Since the two groups are isolated, the resulting magnetic susceptibility is simply given by the sum of the susceptibilities calculated for each group. A correlation between different model parameters depends on the fact that smaller particles have on average stronger temperature dependences and are affected by a larger interaction field.

The model of Fig. 15 has been used to calculate synthetic susceptibility measurements that have been inverted using the method described in Section 4. Results are shown in Fig. 16 for a combination of τ_0 and h_0 that minimizes $\Phi = \langle \delta q^2 \rangle \langle \delta \chi^2 \rangle$. All reconstructed model parameters are intermediate between those assumed for the

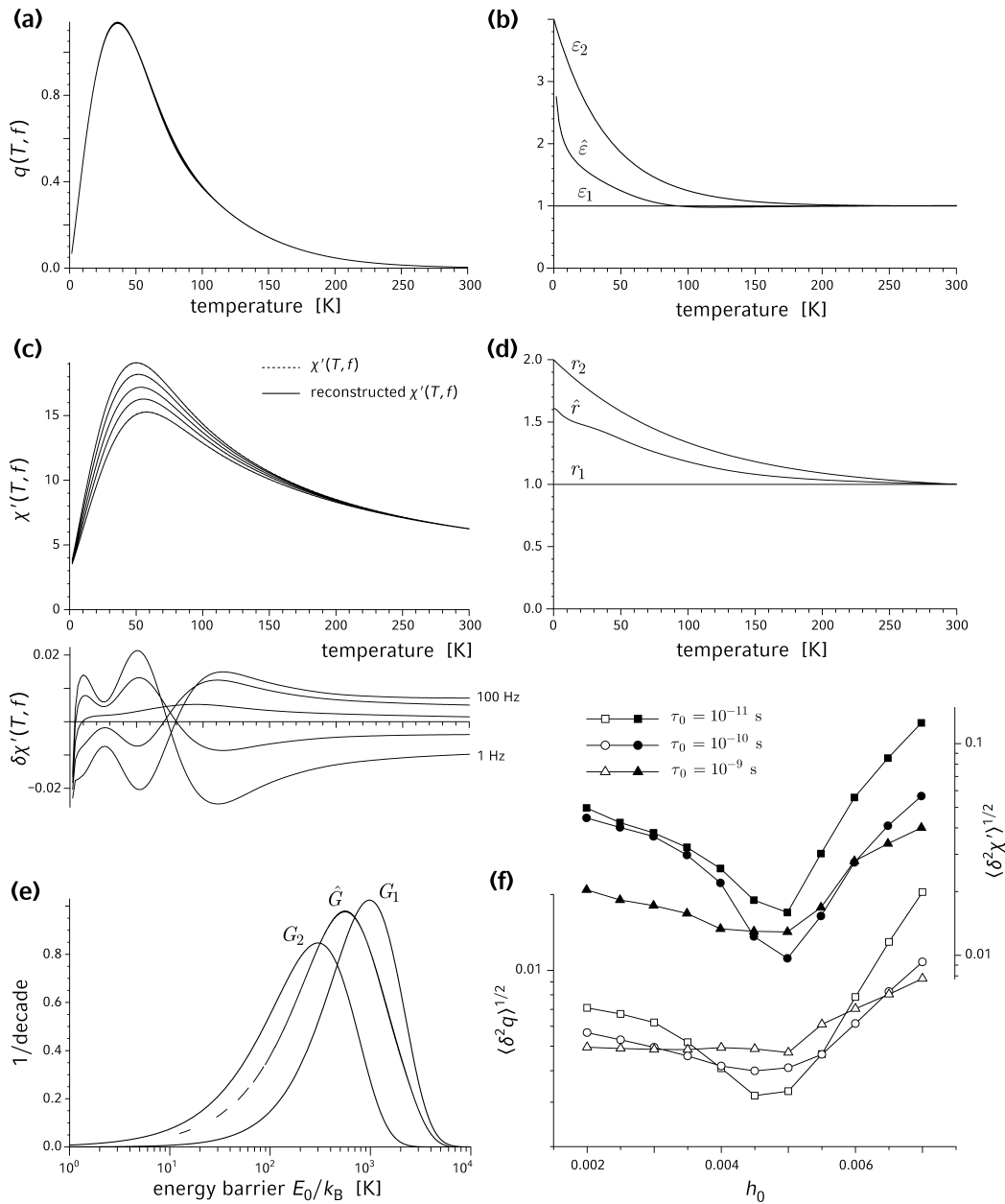


Figure 16. Inversion results for the simulated measurements shown in panels (c) and (d). (a) The functions $q(T, f_j)$ overlap almost perfectly, except for a range of temperatures around 100 K. (b) Estimate $\hat{\varepsilon}(T)$ of $\varepsilon(T)$, compared with the exact parameters $\varepsilon_1(T)$ and $\varepsilon_2(T)$ used to model the two groups of particles. (c) A perfect overlap is obtained between $\chi'(T, f)$ reconstructed from $\chi''(T, f)$ and the simulated measurements. (d) Estimate $\hat{r}(T)$ of $r(T)$, compared with the exact parameters $r_1(T)$ and $r_2(T)$ used to model the two groups of particles. (e) Estimated energy barrier distribution \hat{G} , compared with the distributions used to model the two groups of particles. (f) $\langle \delta^2 q^2 \rangle$ and $\langle \delta^2 \chi^2 \rangle$ are minimized by $\tau_0 \approx 10^{-11}$ s, $h_0 \approx 0.0045$ and $\tau_0 \approx 10^{-10}$ s, $h_0 \approx 0.005$. All estimated model parameters are intermediate between those characterizing the two groups of particles used to calculate the forward model.

two groups of particles in Fig. 15. Although the agreement between simulated measurements and the reconstructed susceptibility is excellent, some inconsistencies exist between the values of τ_0 and h_0 that minimize $\langle \delta^2 \chi^2 \rangle$ and $\langle \delta^2 q^2 \rangle$. For example, a minimum in $\langle \delta^2 \chi^2 \rangle$ is obtained for $h_0 = 0.005$ and $\tau_0 = 10^{-10}$ s, but $\langle \delta^2 q^2 \rangle$ is minimized by $h_0 = 0.0045$ and $\tau_0 = 10^{-11}$ s. The minima of $\langle \delta^2 \chi^2 \rangle$ and $\langle \delta^2 q^2 \rangle$ are also less well defined compared with those obtained for the numerical sample of Fig. 7. Such inconsistencies can be attributed to the correlation between different model parameters.

5.4 Checking susceptibility inversion results

As already discussed, some assumptions of the susceptibility model discussed in Section 3 might not apply to certain categories of SP particles. It is therefore necessary to evaluate the reliability of inverse problem solutions. This can be done by considering three main problems in the interpretation of susceptibility measurements: (1) magnetostatic interactions exceeding the limits of the weak interaction model discussed in 2.3; (2) deviations of the magnetic

relaxation law from the Néel–Brown model (i.e. stretched exponential models) and (3) strong correlations between $r(T)$, $\varepsilon(T)$, h_0 and the volume of the particles. Following checks can help in identifying such problems:

(1) Is $h_0 \leq 0.015$? If not, the forward susceptibility model discussed in Section 3 is probably not correct.

(2) Does the inverse problem have the same solution upon minimization of $\langle \delta\chi^2 \rangle$ and $\langle \delta q^2 \rangle$? If different combinations of h_0 and τ_0 are required to minimize $\langle \delta\chi^2 \rangle$ and $\langle \delta q^2 \rangle$, some model parameters are probably correlated. Solutions of the inverse problem, however, could be interpreted as an average of different individual particle properties.

(3) Does the minimization of $\langle \delta\chi^2 \rangle$ and $\langle \delta q^2 \rangle$ give a realistic estimate of τ_0 ? Values around 10^{-12} and 10^{-10} s are expected for antiferromagnetic and ferrimagnetic particles, respectively. Unrealistic values of τ_0 could be related to strong interactions or to violations of the Néel–Brown relaxation law.

(4) Is the parameter b obtained from susceptibility inversion close to unit for particles whose magnetization is expected to be approximately homogeneous? If not, the Néel–Brown relaxation law does not apply to the system of particles under consideration. This might be due to strong interactions or to a non-uniform reversing mode of the magnetic moment (Wernsdorfer *et al.* 1995).

In a follow-up paper, susceptibility measurements of samples containing SP particles of different compositions are analysed. The inversion results for well-dispersed magnetic particles do pass the criteria (1)–(4) in most cases, suggesting that the susceptibility model discussed in this paper has a general validity.

6 CONCLUSIONS

A method for inverting susceptibility measurements as a function of temperature and frequency has been developed for random assemblies of weakly interacting, uniaxial SP particles. This method represents a generalization of the Shliomis–Stepanov–Raikher model, which accounts for weak magnetostatic interactions and for particles with a magnetization that is not perfectly homogeneous. *A priori* assumptions on the magnetic properties of the particles, as well as model functions describing the distribution of energy barriers, are completely avoided. The only assumption required by the model is that no correlation exists between the temperature dependence of the magnetic moment and the microcoercivity on one hand and the volume of the particles and magnetostatic interactions on the other. Furthermore, the susceptibility model is based on the Néel–Brown relaxation law. The effect of different relaxation laws, such as the stretched exponential, has been investigated.

Estimates of the temperature dependence of magnetic moments and microcoercivities, the mean interaction field, the distribution of energy barriers and the pre-exponential factor in Néel–Brown's relaxation theory can be obtained from the inversion of susceptibility measurements, providing a precise characterization of SP particles. The reliability of the developed inversion method has been tested on numerical samples, whereby the parameters used to generate sets of synthetic susceptibility measurements could be reconstructed accurately.

The inversion of susceptibility data provides an interesting characterization tool to investigate SP particles with known composition on one hand and mixtures of iron nanominerals occurring in natural rocks and sediments on the other. Accurate absolute estimates of the magnetic moment and the anisotropy constant can be obtained for

SP particles of known composition and grain size, determined from independent observations (e.g. electron microscopy). This data provide a useful term of comparison for the analysis of SP particle mixtures occurring in nature. Susceptibility inversion provides also a self-consistency check of existing theories on magnetic relaxation phenomena.

ACKNOWLEDGMENTS

I am indebted to F. J. Lázaro for discussions on relaxation processes in fine magnetic particles and for bringing some of the cited references to my knowledge. The manuscript benefited from helpful remarks by V. Shcherbakov.

REFERENCES

- André, G., Aspelmeier, A., Schulz, B., Farle, M. & Baberschke, K., 1995. Temperature dependence of surface and volume anisotropy in Gd/W(110), *Surf. Sci.*, **326**, 275–284.
- Bae, C.J., Angappane, S., Park, J.G., Lee, Y., Lee, J., An, K. & Hyeon, T., 2007. Experimental studies of strong dipolar interparticle interaction in monodisperse Fe₃O₄ nanoparticles, *Appl. Phys. Lett.*, **91**, 102502.1–102502.3.
- Balanda, M. *et al.*, 2005. Magnetic AC susceptibility of stoichiometric and low zinc doped magnetite single crystals, *Eur. Phys. J. B*, **43**, 201–212.
- Banerjee, S.K., 2006. Environmental magnetism of nanophase iron minerals: testing the biomineralization pathway, *Phys. Earth planet. Inter.*, **154**, 210–221.
- Berkov, D.V. & Gorn, N.L., 2001. Susceptibility of the disordered system of fine magnetic particles: a Langevin-dynamics study, *J. Phys. Condens. Matter*, **13**, 9369–9381.
- Berkowitz, A.E., Lahut, J.A., Jacobs, I.S., Levinson, L.M. & Forester, D.W., 1975. Spin pinning at ferrite-organic interfaces, *Phys. Rev. Lett.*, **34**, 594–597.
- Cornell, R.M. & Schwertmann, U., 2003. *The Iron Oxides*, Wiley VCH, Weinheim.
- Dickson, D.P.E., Reid, N.M.K., Hunt, C., Williams, H.D., El-Hilo, M. & O'Grady, K. 1993. Determination of f_0 for fine magnetic particles, *J. Magn. Magn. Mat.*, **125**, 345–350.
- Dormann, J.L. *et al.*, 1996. Thermal variation of the relaxation time of the magnetic moment of γ -Fe₂O₃ nanoparticles with interparticle interactions of various strengths, *Phys. Rev. B*, **53**, 14 291–14 297.
- Dormann, J.L., Fiorani, D. & Tronc, E., 1997. Magnetic relaxation in fine-particle systems, *Adv. Chem. Phys.*, **98**, 283–494.
- Dunlop, D.J. & Özdemir, Ö., 1997. *Rock Magnetism*, Cambridge University Press, Cambridge.
- Dunlop, D.J. & West, G.F., 1969. An experimental evaluation of single domain theories, *Rev. Geophys.*, **7**, 709–757.
- Egli, R., 2003. Analysis of the field dependence of remanent magnetization curves, *J. geophys. Res.*, **108**, doi:10.1029/2002JB002023.
- Egli, R., 2006. Theoretical aspects of dipolar interactions and their appearance in first-order reversal curves of thermally activated single-domain particles, *J. geophys. Res.*, **111**, B12S17, doi:10.1029/2006JB004567.
- Egli, R. & Lowrie, W., 2002. An hysteretic remanent magnetization of fine magnetic particles, *J. geophys. Res.*, **107**, doi:10.1029/2001JB000671.
- Evans, M.E. & Heller, F., 1994. Magnetic enhancement and paleoclimate: study of a loess/palaeosol couplet across the Loess Plateau of China, *Geophys. J. Int.*, **117**, 257–264.
- Evans, M. E. & Heller, F., 2003. *Environmental Magnetism*, Academic Press, Amsterdam.
- García-Palacios, J.L., 2000. On the statics and dynamics of magnetoanisotropic nanoparticles, *Adv. Chem. Phys.*, **112**, 1–210.
- García-Palacios, J.L. & Lázaro, F.J., 1998. Langevin-dynamics study of the dynamical properties of small magnetic particles, *Phys. Rev. B*, **58**, 14 937–14 958.

- Hansen, M.F., Koch, C.B. & Mørup, S., 2000. Magnetic dynamics of weakly and strongly interacting hematite nanoparticles, *Phys. Rev. B*, **62**, 1124–1135.
- Heslop, D., Dekkers, M.J., Kruijver, P.P. & van Oorschot, I.H.M., 2002. Analysis of isothermal remanent magnetization acquisition curves using the expectation-maximization algorithm, *Geophys. J. Int.*, **148**, 58–64.
- Jackson, M., Carter-Stiglitz, B., Egli, R. & Solheid, P. 2006. Characterizing the superparamagnetic grain distribution $f(V, H_K)$ by thermal fluctuation tomography, *J. geophys. Res.*, **111**, doi:10.1029/2006JB004514.
- Jonsson, T., Mattsson, J., Nordblad, P. & Svedlindh, P., 1997. Energy barrier distribution of a noninteracting nano-sized magnetic particle system, *J. Magn. Magn. Mat.*, **168**, 269–277.
- Jönsson, P.E., 2004. Superparamagnetism and spin glass dynamics of interacting magnetic nanoparticle systems, *Adv. Chem. Phys.*, **128**, 191–248.
- Kappler, A. & Straub, C.L., 2005. Geomicrobiological cycling of iron, *Rev. Mineral. Geochem.*, **59**, 85–108.
- Kodama, R.H., Berkowitz, A.E., McNiff, E.J. & Foner, S., 1996. Surface spin disorder in NiFe₂O₄ nanoparticles, *Phys. Rev. Lett.*, **77**, 394–397.
- Labaye, Y., Crisan, O., Berger, L., Grenèche, J.M. & Coey, J.M.D., 2002. Surface anisotropy in ferromagnetic nanoparticles, *J. appl. Phys.*, **91**, 8715–8717.
- Ledermann, M., Schultz, S., & Ozaki, M., 1994. Measurement of the dynamics of the magnetization reversal in individual single-domain ferromagnetic particles, *Phys. Rev. Lett.*, **73**, 1986–1989.
- Liu, Q., Torrent, J., Maher, B.A., Yu, Y., Deng, C., Zhu, R. & Zhao, X., 2005. Quantifying grain size distribution of pedogenic magnetic particles in Chinese loess and its significance for pedogenesis, *J. geophys. Res.*, **110**, B11102.
- Lu, H.M., Zhao, C.L., Tang, S.C. & Meng, X.K., 2007. Does the nonmagnetic surface layer exist throughout ferromagnetic nanoparticles?, *J. Phys. Chem.*, **111**, 18585–18588.
- Maher, B.A., 1998. Magnetic properties of modern soils and Quaternary loessic paleosols: paleoclimatic implications, *Palaeogeogr. Palaeoclimatol. Palaeoecol.*, **137**, 25–54.
- Moskowitz, B.M., Frankel, R.B., Walton, S.A., Dickson, D.P.E., Wong, K.K.W., Douglas, T. & Mann, S., 1997. Determination of the preexponential frequency factor for superparamagnetic maghemite particles in magnetoferritin, *J. geophys. Res.*, **102**, 22 671–22 680.
- Mørup, S., Madsen, D. E., Frandsen, C., Bahl, C.R.H. & Hansen, M.F., 2007. Experimental and theoretical studies of nanoparticles of antiferromagnetic materials, *J. Phys. Condens. Matter*, **19**, 213202.
- Mullins, C.E. & Tite, M.S., 1973. Magnetic viscosity, quadrature susceptibility, and frequency dependence of susceptibility in single-domain assemblies of magnetite and maghemite, *J. geophys. Res.*, **78**, 804–809.
- Newell, A.J., 2006a. Superparamagnetic relaxation times for mixed anisotropy and high energy barriers with intermediate to high damping, 1: uniaxial axis in a <001> direction, *Geochem. Geophys. Geosyst.*, **7**, Q03016, doi:10.1029/2005GC001146.
- Newell, A.J., 2006b. Superparamagnetic relaxation times for mixed anisotropy and high energy barriers with intermediate to high damping, 2: uniaxial axis in a <111> direction, *Geochem. Geophys. Geosyst.*, **7**, Q03015, doi:10.1029/2005GC001147.
- Néel, L., 1949. Théorie du traînage magnétique des ferromagnétiques en grains fins avec applications aux terres cuites, *Annales de Géophysique*, **5**, 99–136.
- Néel, L., 1961. Superparamagnétisme des grains très fins antiferromagnétiques, *Comptes rendus Academie des Sciences Paris*, **252**, 4075–4080.
- Raikher, Y.L., & Stepanov, V.I., 1997. Linear and cubic dynamic susceptibilities of superparamagnetic fine particles, *Phys. Rev. B*, **55**, 15005–15017.
- Rochette, P., Mathé, P.-E., Esteban, L., Rakoto, H., Bouchez, J.-L., Liu, Q. & Torrent, J., 2005. Non-saturation of the defect moment of goethite and fine-grained hematite up to 57 Teslas, *Geophys. Res. Lett.*, **32**, L22309.
- Sansone, G., 1991. *Orthogonal Functions* (revised English version), Dover, New York.
- Schwartz, M., Lund, S.P. & Hammond, D.E., 1997. Early sediment diagenesis on the Blake/Bahama Outer Ridge, North Atlantic Ocean, and its effects on sediment magnetism, *J. geophys. Res.*, **102**, 7903–7914.
- Seehra, M.S. & Punnoose, A., 2001. Deviations from the Curie-law variation of magnetic susceptibility in antiferromagnetic nanoparticles, *Phys. Rev. B*, **64**, 13 2410-1–13 2410-4.
- Shcherbakov, V. & Fabian, K., 2005. On the determination of magnetic grain-size distributions of superparamagnetic particle ensembles using the frequency dependence of susceptibility at different temperatures, *Geophys. J. Int.*, **162**, 736–746.
- Shendruk, T.N., Desautels, R.D., Southern, B.W. & van Lierop, J., 2007. The effect of surface spin disorder on the magnetism of γ -Fe₂O₃ nanoparticle dispersions, *Nanotechnology*, **18**, 455704.
- Shliomis, M.I. & Stepanov, V.I., 1993. Frequency dependence and long time relaxation of the susceptibility of the magnetic fluids, *J. Magn. Magn. Mat.*, **122**, 176–181.
- Stephenson, A., 1971. Single domain grain size distribution I. A method for the determination of single domain grain distributions, *Phys. Earth planet. Inter.*, **4**, 353–360.
- Stoner, E.C. & Wohlfarth, E.P. 1948. A mechanism of hysteresis in heterogeneous alloys, *Phil. Trans. R. Soc. Lond.*, **240**, 599–602.
- Svedlindh, P., Jonsson, T. & García-Palacios, J.L., 1997. Intra-potential-well contribution to the AC susceptibility of a noninteracting nano-sized magnetic particle system, *J. Magn. Magn. Mat.*, **169**, 323–334.
- Tang, J., Myers, M., Bosnik, K.A. & Brus, L.E., 2003. Magnetite Fe₃O₄ nanocrystals: spectroscopic observation of aqueous oxidation kinetics, *J. Phys. Chem. B*, **107**, 7501–7506.
- Tarduno, J.A., 1995. Superparamagnetism and reduction diagenesis in pelagic sediments: enhancement or depletion?, *Geophys. Res. Lett.*, **22**, 1337–1340.
- Thompson, R. & Oldfield, F., Eds., 1986. *Environmental Magnetism*, Allan and Unwin, London.
- Toll, J.S., 1956. Causality and the dispersion relation: logical foundations, *Phys. Rev.*, **104**, 1760–1770.
- van der Zee, C., Roberts, D.R., Rancourt, D.G. & Slomp, C.P., 2003. Nano-goethite is the dominant reactive oxyhydroxide phase in lake and marine sediments, *Geology*, **31**, 993–996.
- Walz, F., Brabers, V.A.M., Brabers, J.H.V.J. & Kronmüller, H., 2003. Stress-induced relaxation mechanisms in single-crystalline titanomagnetites, *J. Phys. Condens. Matter*, **15**, 7029–7045.
- Wernsdorfer, W., Hasselbach, K., Benoit, A., Cernicchiaro, G., Mailly, D., Barbara, B. & Thomas, L., 1995. Measurement of the dynamics of the magnetization reversal in individual single-domain Co particles, *J. Magn. Magn. Mat.*, **151**, 38–44.
- Wernsdorfer, W. *et al.*, 1997a. Experimental evidence of the Néel-Brown model of magnetization reversal, *Phys. Rev. Lett.*, **78**, 1791–1794.
- Wernsdorfer, W. *et al.*, 1997b. Measurements of magnetization in individual nickel nanowires, *Phys. Rev. B*, **55**, 11552–11559.
- Worm, H.-U., 1998. On the superparamagnetic—stable single domain transition for magnetite, and frequency dependence of susceptibility, *Geophys. J. Int.*, **133**, 201–206.
- Worm, H.-U. & Jackson, M., 1999. The superparamagnetism of Yucca Mountain Tuff, *J. geophys. Res.*, **104**, 25 415–25 425.

APPENDIX

A1 Pre-exponential factor

The high energy barrier approximation of the pre-exponential factor for a magnetic particle with volume V , magnetic moment $m(T)$ and non-relaxing magnetic magnetization $M_{nr} = m/V$ is given by

$$\tau_0 = \frac{\sqrt{\pi}}{4} \frac{m(0)}{\gamma_0 E} \left[\frac{1}{\eta_r} + \eta_r \left(\frac{M_{nr}(T)}{M_{nr}(0)} \right)^2 \right] \left(\frac{E}{k_B T} \right)^{-1/2} \left(1 + \frac{k_B T}{E} \right) \quad (A1)$$

(eq. (1) in Dormann *et al.* 1996). The last term of (A1) can be neglected for large energy barriers. Using $m = VM_{nr}(0)$ and $\beta = E/(k_B T)$ with $E = \mu_0 m H_K/2$ and $\mu = M_{nr}(T)/M_{nr}(0)$ gives eq. (3).

A2 Formulation of the SSR model

The SSR model for identical, aligned SW particles is usually written as

$$\chi = \frac{\chi_{\parallel}}{1 + i\omega\tau_{\parallel}} \cos^2 \alpha + \frac{\chi_{\perp}}{1 + i\omega\tau_{\perp}} \sin^2 \alpha, \quad (\text{A2})$$

where α is the angle between the easy axes and the applied field, and

$$\chi_{\parallel} = \frac{\mu_0 m^2}{k_B T} \frac{1 + 2\tilde{S}_2}{3}, \quad \chi_{\perp} = \frac{\mu_0 m^2}{k_B T} \frac{1 - \tilde{S}_2}{3} \quad (\text{A3})$$

are the so-called equilibrium susceptibilities, with $(1 + 2\tilde{S}_2)/3 = \xi$ (eqs 3.75 and 4.2 in García-Palacios 2000). In the low-frequency case, $\omega\tau_{\perp} \ll 1$. Substituting β in (A3), and integrating over all angles gives the susceptibility

$$\chi = \frac{2m}{H_K} \frac{\beta\xi}{1 + i\omega\tau_{\parallel}} \frac{1}{2} \int_0^{\pi} \cos^2 \alpha \sin \alpha \, d\alpha + \frac{2m}{H_K} \frac{1 - \xi}{2} \frac{1}{2} \int_0^{\pi} \sin^3 \alpha \, d\alpha \quad (\text{A4})$$

of randomly oriented particles. Eqs (4) and (5) follow immediately from (A3) if m is replaced by M_s .

A3 Energy barrier distribution

The EBD $G(E_0)$ (as defined in Section 3.4) is the contribution of all particles with a given energy barrier E_0 to the susceptibility $\chi_0 \propto m/H_K$ of the sample. The energy barrier itself is the function of a set of independent variables describing the magnetic properties of the particles. In the case of SW particles, the independent variables can be chosen to be the grain volume V and the microcoercivity H_K , and a set of particles with identical composition is fully described by the joint grain distribution $f(V, H_K)$ (as defined in Jackson *et al.* 2006) as the contribution of all particles with a given volumes V and microcoercivities H_K to the magnetization of the sample, which is $\propto m$. Since $\chi_0 \propto m/H_K$ and $f(V, H_K) \propto m$, $G(E_0)$ is obtained by integrating $f(V, H_K)/H_K$ over all (V, H_K) pairs corresponding to the same E_0 . Using $E_0 = \mu_0\mu_s V H_K/2$,

$$G(E_0) = \frac{1}{E_0} \int_0^{\infty} f(V, H_K) \, dV \quad (\text{A5})$$

with $H_K = 2E_0/(\mu_0\mu_s V)$. The joint distribution can be written as $f = v(V)s(H_K, V)$, where v is the volume distribution and s is the microcoercivity distribution. If the microcoercivity distribution is much narrower than the volume distribution, $s(H_K, V)$ can be approximated with a Dirac δ -function centred on the average microcoercivity $\bar{H}_K(V)$ of all particles with volume V . A further simplification is obtained if \bar{H}_K is assumed to be independent of V . In this case, (A5) simplifies to

$$v(V) = \frac{\mu_0\mu_s \bar{H}_K^2}{2} G(\mu_0\mu_s V \bar{H}_K/2). \quad (\text{A6})$$

In case of a bimodal mixture of particles with two different values of \bar{H}_K , it is clear from (A6) that the relative contribution of each group of particles to G and v is different.

A4 Proof of eq. (14)

After substituting (13) with $f = f_1$ into (11) with $f = f_0$ and assuming $\xi_b = 1$, one obtains

$$\chi''(T, f_0) = \frac{r(T)}{r(u)} \chi''(u; f_1) \frac{J[2h_0 r(T) \ln w_0]}{J[2h_0 r(u) \ln w_1]}, \quad (\text{A7})$$

$$\frac{u}{\varepsilon(u)} = \frac{T}{\varepsilon(T)} \frac{\ln w_0}{\ln w_1}.$$

If all terms containing T are brought to the right-hand side of (A7), eq. (14) is obtained.

A5 Proof of the $\pi/2$ -law

Using (14), eq. (16) can be written as

$$\chi'_{sw}(T, f) = \frac{2}{\pi \xi_b} \int_0^{-\ln w} q(u) r(T) \xi(\beta) J[2h_0 r(T) \beta] \, d\beta, \quad (\text{A8})$$

with u being the solution of (17). Since $q(u)$, and thus the entire expression inside the integral, is independent of f , the derivative of (A8) with respect to $\ln w$ is simply given by applying Leibnitz's rule:

$$\chi_f = \frac{2}{\pi} \chi''(u, f) \frac{r(T)}{r(u)} \frac{\xi(\beta)}{\xi_b} \frac{J[2h_0 r(T) \beta]}{J[2h_0 r(u) \ln w]} \Big|_{\beta=-\ln w}, \quad (\text{A9})$$

$$\frac{u}{\varepsilon(u)} = - \frac{T}{\varepsilon(T)} \frac{\beta}{\ln w} \Big|_{\beta=-\ln w}.$$

The second line of (A9) simplifies to $u/\varepsilon(u) = T/\varepsilon(T)$, which has the trivial solution $u = T$. If this solution is substituted into the first line of (A9), (18) follows immediately.

A6 Proof of eqs (19) and (20)

Using (17), one can calculate the derivative of u with respect to β :

$$\frac{\partial u}{\partial \beta} = - \frac{T}{\varepsilon(T)} \frac{1}{\ln w} \left[\frac{1}{\varepsilon(u)} - \frac{u}{\varepsilon^2(u)} \varepsilon'(u) \right]^{-1}, \quad (\text{A10})$$

and rewrite (16) using the substitution rule $du = (\partial u/\partial \beta) \, d\beta$:

$$\chi'_{sw}(T, f) = \frac{2}{\pi \xi_b} \int_0^T (u, f) \frac{r(T)}{r(u)} \xi(\beta) \frac{J[2h_0 r(T) \beta]}{J[2h_0 r(u) \ln w]} \frac{\partial \beta}{\partial u} \, du. \quad (\text{A11})$$

Eq. (19) is obtained from (A11) after solving (17) with respect to β , then substituting β with the resulting expression and $\partial \beta/\partial u$ with the reciprocal of (A10). Similarly, the first integral in (8) is first rewritten by substituting $G(E_0)$ with (13), obtaining

$$\kappa = \frac{2r(T)}{\pi \xi_b} \int_{\infty}^0 \frac{\chi''(u; f)}{r(u) \beta J[2h_0 r(u) \ln w]} \eta(\beta) \, d\beta. \quad (\text{A12})$$

Eq. (20) follows after substituting β with u .

A7 Proof of eqs (21) and (23)

A set f_1, f_2, \dots, f_n of n functions is linearly independent in a given interval I if the Wronskian determinant $W(f_1, f_2, \dots, f_n)$ with

$$W = \begin{vmatrix} f_1 & f_2 & \cdots & f_n \\ f_1' & f_2' & \cdots & f_n' \\ \vdots & \vdots & \ddots & \vdots \\ f_1^{(n-1)} & f_2^{(n-1)} & \cdots & f_n^{(n-1)} \end{vmatrix} \quad (\text{A13})$$

is not zero for at least one $x \in I$. Considering $\chi_p \delta p$ as functions of f , the corresponding Wronskian determinant can be written as

$$W = \begin{vmatrix} \chi_\varepsilon \delta \varepsilon & \chi_r \delta r & \chi_h \delta h_0 & \chi_\tau \delta \ln \tau_0 \\ \partial_f \chi_\varepsilon \delta \varepsilon & \partial_f \chi_r \delta r & \partial_f \chi_h \delta h_0 & \partial_f \chi_\tau \delta \ln \tau_0 \\ \partial_f^2 \chi_\varepsilon \delta \varepsilon & \partial_f^2 \chi_r \delta r & \partial_f^2 \chi_h \delta h_0 & \partial_f^2 \chi_\tau \delta \ln \tau_0 \\ \partial_f^3 \chi_\varepsilon \delta \varepsilon & \partial_f^3 \chi_r \delta r & \partial_f^3 \chi_h \delta h_0 & \partial_f^3 \chi_\tau \delta \ln \tau_0 \end{vmatrix}, \quad (A14)$$

where ∂_f^n is the n th derivative with respect to f . Since the δp s do not depend on f , they are scalar constants that can be extracted from the determinant. Therefore, the Wronskian determinant given in eq. (21) is proportional to (A12). Eq. (21) was then evaluated analytically using Mathematica[®] and (11) and (12).

Solution of eq. (22) with respect to δr gives

$$\delta r = \frac{\chi_\varepsilon \delta \varepsilon - \chi_h \delta h_0 - \chi_\tau \delta \ln \tau_0}{\chi_r}. \quad (A15)$$

Since $r = r(T) \in \mathbb{R}$, δr must be a real function that is independent of f , that is, $\text{Im}(\delta r) = 0$ and $\partial(\delta r)/\partial f = 0$. These two conditions give

$$\begin{cases} (\chi'_\varepsilon \delta \varepsilon - \chi'_h \delta h_0 - \chi'_\tau \delta \ln \tau_0) \chi'_r \\ -(\chi''_\varepsilon \delta \varepsilon - \chi''_h \delta h_0 - \chi''_\tau \delta \ln \tau_0) \chi_r = 0, \\ (\chi_{\varepsilon,f} \delta \varepsilon - \chi_{h,f} \delta h_0 - \chi_{\tau,f} \delta \ln \tau_0) \chi_r \\ -(\chi_\varepsilon \delta \varepsilon - \chi_h \delta h_0 - \chi_\tau \delta \ln \tau_0) \chi_{r,f} = 0. \end{cases} \quad (A16)$$

Both equations in (A16) can be solved with respect to $\delta \varepsilon$, obtaining the two solutions:

$$\begin{aligned} \delta \varepsilon^I &= \frac{(\chi'_h \chi_r'' - \chi''_h \chi_r') \delta h_0 + (\chi'_\tau \chi_r'' - \chi''_\tau \chi_r') \delta \ln \tau_0}{\chi'_\varepsilon \chi_r'' - \chi''_\varepsilon \chi_r'}, \\ \delta \varepsilon^{II} &= \frac{(\chi_{h,f} \chi_r - \chi_h \chi_{r,f}) \delta h_0 + (\chi_{\tau,f} \chi_r - \chi_\tau \chi_{r,f}) \delta \ln \tau_0}{\chi_{\varepsilon,f} \chi_r - \chi_\varepsilon \chi_{r,f}}. \end{aligned} \quad (A17)$$

Since $\varepsilon = \varepsilon(T) \in \mathbb{R}$, $\delta \varepsilon$ must be a real function that is independent of f . Hence, $\partial(\delta \varepsilon^I)/\partial f = 0$, $\text{Im}(\delta \varepsilon^{II}) = 0$ and $\partial(\delta \varepsilon^{II})/\partial f = 0$. The last condition involves second derivatives of f , and assuming these to be zero, it is automatically fulfilled. The first two conditions can be met only if $\delta \varepsilon^I$ is constant in the frequency domain and $\delta \varepsilon^{II}$ is constant in the temperature domain. This is only possible if the terms that multiply δh_0 and $\delta \tau_0$ in $\delta \varepsilon^I$ and $\delta \varepsilon^{II}$ are linearly dependent. Linear dependence imply that they are proportional to each other, or in other words, that their ratios are constant. Eq. (23) follows immediately by requiring these ratios to be constant in the frequency domain (i.e. $\partial/\partial f = 0$ for the case of $\delta \varepsilon^I$) or in the temperature domain (i.e. $\partial/\partial T = 0$ for the case of $\delta \varepsilon^{II}$).

A8 Proof of eqs (25) and (27)

If $u/T \rightarrow 1$, one can write $u = (1 + \delta)T$ with $\delta \rightarrow 0$. Eq. (15) is then linearized with respect to δ , obtaining

$$\delta(T) = \frac{\lambda - 1}{1 - T \varepsilon'(T)/\varepsilon(T)}. \quad (A18)$$

Using $s = \delta/(\lambda - 1)$, (25) is obtained. Rearranging (A18) and substituting δ with $(\lambda - 1)s$ gives the following differential equation:

$$\frac{\varepsilon'(T)}{\varepsilon(T)} = \frac{1}{T} \left[\frac{1}{s(T)} - 1 \right]. \quad (A19)$$

(A19) is solved by integration with respect to T , obtaining:

$$\ln \varepsilon(T) = A + \int \frac{dT}{Ts(T)} - \ln T, \quad (A20)$$

where A is an integration constant to be chosen, so that $\varepsilon(T_0) = 1$. Eq. (27) follows from (A20) after A is calculated.

The stability of (27) at $T \rightarrow 0$ can be investigated by approximating $s(T)$ with the Mc Laurin series $s(T) = s(0) + s'(0)T + \mathcal{O}(T^2)$. Following limit solution is then obtained:

$$\lim_{T \rightarrow 0} \varepsilon(T) = \left(\frac{T}{T_0} \right)^{1-1/s(0)} \left(\frac{s(0) + s'(0)T}{s(0) + s'(0)T_0} \right)^{1/s(0)}. \quad (A21)$$

(A21) does not diverge at $T = 0$ only if $s(0) > 1$. Therefore, $\varepsilon(T \rightarrow 0)$ is very sensitive to measurement errors if $s(0) \rightarrow 1$.

A9 Proof of eq. (31)

Linearization of (19) with respect to ρ_i , obtained after ignoring the dependence of the cosh terms on r , gives

$$\begin{aligned} \Delta \chi'_{sw}(T, f, r_i) &= \frac{2 \ln w}{\pi T \xi_b} \int_0^T \chi''(u, f) \frac{r_i(T) \varepsilon(T)}{r_i(u) \varepsilon(u)} [\rho_i(T) - \rho_i(u)] \\ &\times \left[1 - u \frac{\varepsilon'(u)}{\varepsilon(u)} \right] \frac{J(\dots)}{J(\dots)} \xi \dots du. \end{aligned} \quad (A22)$$

Eq. (A22) is rearranged to obtain

$$\begin{aligned} \frac{T \Delta \chi'_{sw,i}(T, f)}{r_i(T) \varepsilon(T)} &= \frac{2 \ln w}{\pi \xi_b} \\ &\times \int_0^T \chi''(u, f) \frac{\rho_i(T) - \rho_i(u)}{r_i(u) \varepsilon} \left[1 - u \frac{\varepsilon'(u)}{\varepsilon(u)} \right] \frac{J(\dots)}{J(\dots)} du. \end{aligned} \quad (A23)$$

The derivative of (A23) with respect to T is

$$\frac{\partial}{\partial T} \frac{T \Delta \chi'_{sw,i}(T, f)}{r_i(T) \varepsilon(T)} = \frac{2 \ln w}{\pi \xi_b} \rho'_i(T), \quad (A24)$$

$$\times \int_0^T \frac{\chi''(u, f)}{r_i(u) \varepsilon(u)} \left[1 - u \frac{\varepsilon'(u)}{\varepsilon(u)} \right] \frac{J(\dots)}{J(\dots)} \xi(\dots) du,$$

where ρ'_i is the derivative of ρ_i with respect to T . Since $r_i \approx r$, the integral in (A24) can be identified with χ'_{sw} , and (31) follows.